The Quest for B Modes from Inflationary Gravitational Waves

Marc Kamionkowski and Ely D. Kovetz

Department of Physics and Astronomy, Johns Hopkins University, 3400 N. Charles St., Baltimore, Maryland, 21218, USA

Abstract

The search for the curl component (B mode) in the cosmic microwave background (CMB) polarization induced by inflationary gravitational waves is described. The canonical single-field slow-roll model of inflation is presented, and we explain the quantum production of primordial density perturbations and gravitational waves. It is shown how these gravitational waves then give rise to polarization in the CMB. We then describe the geometric decomposition of the CMB polarization pattern into a curl-free component (E mode) and curl component (B mode) and show explicitly that gravitational waves induce B modes. We discuss the B modes induced by gravitational lensing and by Galactic foregrounds and show how both are distinguished from those induced by inflationary gravitational waves. Issues involved in the experimental pursuit of these B modes are described, and we summarize some of the strategies being pursued. We close with a brief discussion of some other avenues toward detecting/characterizing the inflationary gravitational-wave background.

Contents

1. Introduction

The daily vistas encountered by the inhabitants of Earth feature seashores, mountains, cliffs, ice, fire, raging storms, and a sky that meets the ground through a horizon that may be jagged or straight. Our astronomical vista is similarly complex, with a startling display of stars, binary stars, compact objects, intergalactic gases and dust, an array of galaxies, and clusters of galaxies, no two of which look precisely alike. Our cosmic vista, however, is far simpler. When we look to the greatest observable cosmic distances, the Universe is virtually the same everywhere, with only tiny departures from homogeneity. It turns out that these subtle inhomogeneities, which through heroic experimental efforts have now been mapped with formidable precision, exhibit nontrivial but still surprisingly simple patterns. According to the standard cosmological model, these are seeded by primordial quantum perturbations that are imprinted onto the early Universe by a process of rapid exponential expansion known as inflation.

The era of precision cosmology was ushered in during the past decade by ever more accurate measurements of the distribution of mass in the Universe on cosmic distance scales using galaxy surveys (Dawson et al. 2013; Amendola et al. 2013) and through measurements of temperature fluctuations and polarization in the cosmic microwave background (CMB) (Bennett et al. 2013; Adam et al. 2015a). Together, these measurements indicate that the early Universe was homogeneous to better than one part in 10,000. They indicate that departures from homogeneity are "adiabatic"—i.e., they preserve the ratios of the different components of matter (baryons, dark matter, radiation, and neutrinos) in the Universe. As discussed below, the primordial inhomogeneities (which hereafter we refer to as density perturbations) are well described by an impressively simple structure, a nearly

scale-invariant spectrum with a Gaussian distribution of Fourier amplitudes.

The goal of early-Universe cosmology is to quantify the observed features of the Universe and to develop a physical model to account for them. Up until several decades ago, the number of such models was huge, and they made a large array of predictions for the nature of primordial perturbations: for the Fourier-space spectrum; for correlations between the different Fourier amplitudes; for spatial structures like cosmic strings, textures, and monopoles; for fluctuations in the ratios of baryons, dark matter, radiation, and/or neutrinos, etc. Today, the vast majority of these models are dead, ruled out by the onslaught of precise measurements. The overwhelming majority of those that survive involve inflation (Brout, Englert & Gunzig 1978; Starobinsky 1980; Kazanas 1980; Sato 1981; Guth 1981; Linde 1982a; Albrecht & Steinhardt 1982), a period of accelerated expansion in the very early Universe (within the first fraction of a nanosecond of the Universe), and explain primordial perturbations as quantum fluctuations in the spacetime metric during inflation (Mukhanov & Chibisov 1981; Hawking 1982; Guth & Pi 1982; Starobinsky 1982; Linde 1982b; Bardeen, Steinhardt & Turner 1983).

The simplest and canonical model for inflation—namely single-field slow-roll (SFSR) inflation—made a number of predictions that have been confirmed by a sequence of increasingly precise experiments over the past two decades. These include the prediction that (a) primordial perturbations are adiabatic; (b) the spectrum of primordial perturbations should be very nearly scale invariant, but not precisely scale invariant; (c) the distribution of primordial perturbations should be very nearly Gaussian; and (d) there should be primordial perturbations that are super-horizon (i. e. with wavelengths larger than the Hubble radius) at the time of CMB decoupling. The consistency of these predictions with all current cosmological data suggests that inflation is an idea that should be taken seriously and studied further.

Still, inflation raises its own set of questions (e.g., what set it in motion?), and the literature is teeming with detailed implementations. The focus of early-Universe cosmology in the forthcoming years will be to further test the notion of inflation and narrow the range of inflationary models and scenarios. Given that we are talking about physics from 13.8 billion years ago, when the relevant energy scales were well beyond those at accelerator laboratories, this is an ambitious quest. Since observable fossils from that time are few and far between, any conceivable empirical avenue to inflation should be pursued.

In addition to the predictions for primordial density perturbations discussed above, SFSR inflation also predicts the existence of a stochastic background of gravitational waves (Starobinsky 1979; Rubakov, Sazhin & Veryaskin 1982; Fabbri & Pollock 1983; Abbott & Wise 1984) that then induce a specific gradient-free "B-mode" pattern in the polarization of the CMB (Kamionkowski, Kosowsky & Stebbins 1997a; Seljak & Zaldarriaga 1997; Kamionkowski, Kosowsky & Stebbins 1997b; Zaldarriaga & Seljak 1997; Seljak 1997). This review focuses on these B modes and their role in addressing the physics of inflation. When first considered in 1996, the amplitude of these B modes could have been just about anything, in the best-case scenario easily detectable and in the worst-case scenario way too small to ever be seen. As we shall discuss, though, recent measurements of the spectral index (Knox 1995; Jungman et al. 1996; Komatsu et al. 2009; Calabrese et al. 2013; Ade et al. 2014e, 2015c) suggest, within the context of SFSR inflation, that the B-mode signal may be strong enough to be detectable by experiments planned for the next 5–10 years, making this a particularly exciting time.

Below we begin by reviewing the basics of inflation, starting with the homogeneous

cosmic evolution during inflation and then discussing the generation of density perturbations and gravitational waves. We discuss how gravitational waves produce polarization in the CMB, and then describe the decomposition of the polarization pattern into two distinct geometric components, a curl-free (E mode) part and a curl (B mode) part. We do so first within the context of a flat-sky approximation before moving to the full-sky formalism. Next, we show explicitly that gravitational waves give rise to B modes while primordial density perturbations do not (at linear order in the perturbation amplitude). We then discuss the B modes induced by lensing of the CMB by density inhomogeneities along the line of sight (Zaldarriaga & Seljak 1998) and also how these lensing-induced B modes can be distinguished from primordial B modes (Kesden, Cooray & Kamionkowski 2002; Knox & Song 2002). The remainder of the article discusses the detectability of the signal, strategies for detection, and issues involved in separating a cosmic signal from that due to Galactic foregrounds. We close with a brief discussion of some other avenues toward detection and characterization of the inflationary gravitational-wave background.

Before proceeding with our review, we provide an incomplete list of reviews of related subjects. An early review (Brandenberger 1985) and much of the formalism for cosmological perturbations was elaborated in (Kodama & Sasaki 1984; Mukhanov, Feldman & Brandenberger 1992; Bertschinger 1993) and then updated in (Malik & Wands 2009). Olive (1990) reviewed inflation models around 1990 followed by Lyth & Riotto (1999) in 1997. Lidsey et al. (1997) reviewed single-field slow-roll inflation and then several more recent articles review models for inflation beyond single-field slow roll. These include a review of curvaton models (Mazumdar & Rocher 2011), one about models with gauge fields (Maleknejad, Sheikh-Jabbari & Soda 2013), and others of models that embed inflation in string theory (Baumann & McAllister 2009, 2015; Westphal 2015). Martin, Ringeval & Vennin (2014) classifies a broad range of inflationary models. Bartolo et al. (2004) discusses non-gaussianity and inflation. The recent Planck inflation papers (Ade et al. 2014g, 2015d) also provide very nice up-to-date discussions of inflation. Kamionkowski & Kosowsky (1999) reviewed connections between particle physics and the CMB; Hu & Dodelson (2002) reviewed the theory of CMB fluctuations; and Lewis & Challinor (2006) discussed lensing of the CMB. Hu & White (1997a) provided a short but elegant early review of CMB polarization, and this review builds and expands upon an earlier review (Cabella & Kamionkowski 2004). The review of Samtleben, Staggs & Winstein (2007) on CMB polarization complements this review in its deeper coverage of experimental techniques. Finally, Buonanno & Sathyaprakash (2014) provides a recent review of the direct search for gravitational waves.

2. Inflation basics

Inflation has become such a dominant paradigm that we often forget the original motivations—the flatness problem (why is the present ratio of the energy density relative to the critical energy density so close to unity?), the horizon problem (why do causally disconnected regions at the CMB surface of last scatter have the same temperature), and the monopole problem (Preskill 1979)—at the time, ~ 1980, that the idea began to take shape. The solution to all these problems was provided by a postulated period of accelerated expansion in the early Universe (Guth 1981).

2.1. Homogeneous evolution

2.1.1. Kinematics. An expanding isotropic and homogeneous Universe is described by a Friedmann-Robertson-Walker (FRW) spacetime, with line element $ds^2 = -dt^2 + a^2(t)d\boldsymbol{x}^2$, in terms of a scale factor $a(t)$ that parametrizes the physical distance that corresponds to a given comoving distance. As the Universe expands [i.e., the scale factor $a(t)$ increases with time t], the Hubble length H^{-1}, where $H \equiv \dot{a}/a$ is the Hubble or growth rate, increases. During radiation and matter domination, $(d/dt)(aH)^{-1} > 0$, and so the Hubble distance H^{-1} increases more rapidly than the scale factor. As a result, with time, an observer sees larger comoving volumes of the Universe, and objects and information enter the horizon. This observation leads to the horizon problem: if the Universe began with a period of radiation domination, then how did the $\sim 40,000$ causally disconnected patches of CMB sky know to have the same temperature (to roughly one part in 10,000)?

If, however, $(d/dt)(aH)^{-1} < 0$, then an observer sees with time a smaller comoving patch (even though the physical or proper size of the observable patch may still be increasing), and objects/information/perturbations exit the horizon. In this way, the Universe becomes increasingly smooth, thus explaining the remarkable large-scale homogeneity of the Universe.

The requirement $(d/dt)(aH)^{-1} = \left[(\dot{H}/H^2) + 1 \right]/a < 0$, where the dot denotes a derivative with respect to time, implies that we must have $\epsilon \equiv -\dot{H}/H^2 < 1$ for inflation. Most generally, $\dot{H} \neq 0$ (so that inflation can end, if for no other reason). As we will see, however, theory and measurement suggest $\epsilon \ll 1$, implying that the scale factor grows almost exponentially, $a(t) \propto e^{Ht}$, during inflation.

If we assume the validity of general relativity, as we do here [although there is a vast literature on inflation with alternative gravity theories; e.g., La & Steinhardt (1989); De Felice & Tsujikawa (2011); Clifton et al. (2012)], then the time evolution of the scale factor satisfies the Friedmann equations, $H^2 = \rho/(3M_{\mathrm{Pl}}^2)$ and $\dot{H} + H^2 = -(\rho + 3p)/(6M_{\mathrm{Pl}}^2)$, where p and ρ are the pressure and energy density of the cosmic fluid, respectively. We work in particle-physics units, with $\hbar = c = 1$ and have written Newton's constant $G = (8\pi M_{\mathrm{Pl}}^2)^{-1}$ in terms of the reduced Planck mass, $M_{\mathrm{Pl}} = 2.435 \times 10^{18}$ GeV. These two Friedmann equations imply that

$$\epsilon = (3/2)\left(1 + p/\rho\right), \tag{1}$$

from which we infer that the equation-of-state parameter $w \equiv p/\rho$ must be $w < -1/3$ in order for inflation to occur.

2.1.2. Scalar-Field Dynamics. In the simplest paradigm for inflation, and that on which we focus, this exotic equation of state is provided by the displacement of a scalar field ϕ, the "inflaton," from the minimum of its potential $V(\phi)$. The homogeneous time evolution of the scalar field then satisfies, in an FRW spacetime, the equation of motion, $\ddot{\phi} + 3H\dot{\phi} + V'(\phi) = 0$, where the prime denotes a derivative with respect to ϕ. We thus see that the expansion acts as a friction term. The scalar field has energy density $\rho = (1/2)\dot{\phi}^2 + V(\phi)$ (a kinetic-energy density and a potential-energy density) and pressure $p = (1/2)\dot{\phi}^2 - V(\phi)$. If $V(\phi)$ is nonzero and sufficiently flat and the friction term in the ϕ equation sufficiently large, then the kinetic-energy density will be $(1/2)\dot{\phi}^2 < 2V(\phi)$, in which case $p < -\rho/3$ and inflation ensues (see **Figure 1**).

This condition is made more precise by solving the scalar-field equation of motion along with the Friedmann equation, $H^2 = (\dot{a}/a)^2 = \left[V(\phi) + (1/2)\dot{\phi}^2 \right]/(3m_{\mathrm{Pl}}^2)$. During inflation
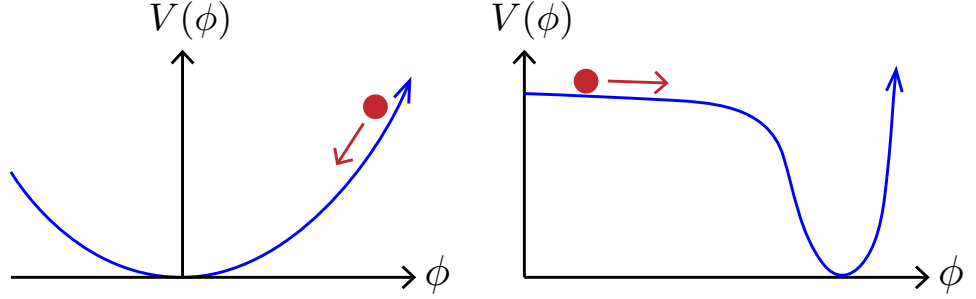
Inflation postulates that at some point in the early history of the Universe, the cosmic energy density was dominated by the vacuum energy associated with the displacement of some scalar field ϕ (the inflaton) from the minimum of its potential. Shown here for illustration are two toy models for the inflaton potential: on the left, a quadratic potential and on the right, a hilltop potential. (Adapted from Kamionkowski & Kosowsky (1999)).

ϕ varies monotonically with time t and can thus be used as the independent variable (rather than t). Let us suppose that the field and potential are defined so that $\dot{\phi} > 0$ during inflation. We then differentiate the Friedmann equation with respect to time, obtaining $2H\dot{H} = \dot{\phi}\left[V'(\phi) + \ddot{\phi}\right]/(2m_{\mathrm{Pl}}^2)$. Then rearranging the scalar-field equation of motion, $-3H\dot{\phi} = \ddot{\phi} + V'(\phi)$, we get $\dot{H} = \dot{\phi}^2/(2m_{\mathrm{Pl}}^2)$. We thus infer that

$$\epsilon = 3\frac{\dot{\phi}^2/2}{V + \dot{\phi}^2/2} \simeq \frac{M_{\mathrm{Pl}}^2}{2}\left(\frac{V'}{V}\right)^2, \tag{2}$$

where the last expression is the result of the slow-roll approximation, $\epsilon \ll 1$, in which $\dot{\phi}^2/2 \ll V$. Note that in much of the literature, ϵ is *defined* in terms of V and V' through this relation, rather than through $\epsilon = -\dot{H}/H^2$, as is done here, a distinction whose subtlety will be unimportant in this article, although it can be important for quantitative conclusions given the precision of current measurements. We also define a second slow-roll parameter,

$$\eta = -2\frac{\dot{H}}{H^2} - \frac{\dot{\epsilon}}{2H\epsilon} \simeq M_{\mathrm{Pl}}^2\frac{V''}{V}, \tag{3}$$

which will become important below; the approximation in Equation 3 is valid during slow-roll, when $\eta \ll 1$.

2.1.3. Duration of inflation and evolution of scales. The number of e-folds of inflation between the end of inflation and a time t during inflation is

$$N(t) \equiv \ln\frac{a(t_{\mathrm{end}})}{a(t)} = \int_t^{t_{\mathrm{end}}} H\,dt = -\frac{1}{2m_{\mathrm{Pl}}^2}\int_{\phi_t}^{\phi_{\mathrm{end}}} \frac{H}{H'}\,d\phi = \int_{\phi_{\mathrm{end}}}^{\phi_t} \frac{d\phi}{M_{\mathrm{Pl}}}\frac{1}{\sqrt{2\epsilon(\phi)}}. \tag{4}$$

The largest comoving scales exit the horizon first during inflation, and they are the last to re-enter the horizon later during matter or radiation domination. To evaluate the number of e-foldings required to solve the horizon problem, consider a physical wavenumber k_{phys}. Its ratio to the Hubble scale today is

$$\frac{k_{\mathrm{phys}}}{a_0 H_0} = \frac{a_k H_k}{a_0 H_0} = \frac{a_k}{a_{\mathrm{end}}}\frac{a_{\mathrm{end}}}{a_{\mathrm{reh}}}\frac{a_{\mathrm{reh}}}{a_{\mathrm{eq}}}\frac{a_{\mathrm{eq}}}{a_0}\frac{H_k}{H_0}, \tag{5}$$

Heuristic understanding of inflationary gravitational waves. Here we present in simple heuristic terms the origin of inflationary gravitational waves (IGWs). Consider first a black hole. As shown in **Figure 2**, it has an event horizon, a spherical surface beyond which, according to (classical) general relativity, objects and information disappear without a trace. Hawking showed, however, that when quantum mechanics is taken into consideration, the horizon glows—it emits electromagnetic radiation (Hawking 1975). Hawking's argument also applies, however, to any radiation field with massless quanta, and so the black hole also radiates gravitational waves. In an FRW Universe with an accelerated expansion, there is also a horizon, a spherical surface beyond which (according to general relativity) objects and information disappear. This time, though, the observer sees this spherical surface from the inside, rather than outside. Just as was the case with the black-hole horizon, this horizon also radiates gravitational waves, according to quantum mechanics. These gravitational waves are produced throughout inflation, and the expansion rate and thus horizon temperature are nearly constant during inflation. These gravitational waves thus remain, after inflation, as a primordial-gravitational-wave background with a nearly scale-invariant spectrum.

where a_k and H_k are the scale factor and Hubble parameter when this particular wavenumber exits the horizon; $a_{\rm end}$ is the scale factor at the end of inflation; $a_{\rm eq}$ is the scale factor at matter-radiation equality; and $a_{\rm eh}$ is the scale factor at the time of reheating. Plugging in numbers, we find that the number of e-foldings between the end of inflation and the time at which the wavenumber k exits the horizon is

$$N(k) = 62 - \ln \frac{k_{\rm phys}}{a_0 H_0} - \ln \frac{10^{16}\,{\rm GeV}}{V_k^{1/4}} + \ln \frac{V_k^{1/4}}{V_{\rm end}} - \frac{1}{3} \ln \frac{V_{\rm end}^{1/4}}{\rho_{\rm reh}^{1/4}}, \qquad (6)$$

where $\rho_{\rm reh}^{1/4}$ is the energy density at reheating. If the energy scale of inflation is near the current upper limit $V^{1/4} \lesssim 10^{16}$ GeV (see below), but higher than the energy scale of electroweak symmetry breaking ($V_k \gtrsim 10^3$ GeV), then the number N of e-folds between the time that the largest observable scales today exited the horizon and the end of inflation falls in the range $30 \lesssim N \lesssim 60$. Recent treatments that consider different families of inflationary potentials, include current constraints to the scalar spectral index n_s (see below), as well as plausible reheating scenarios, find a range $40 \lesssim N \lesssim 60$ (Dai, Kamionkowski & Wang 2014; Cook et al. 2015; Munoz & Kamionkowski 2015). More conservatively, the near scale-invariance of primordial density perturbations over the ~ 3 orders of magnitude over which they have been measured tells us that $N \gtrsim 10$ at the very least.

2.2. Density (scalar metric) perturbations

We now discuss the production of primordial density perturbations from quantum fluctuations in the inflaton. Although this involves a straightforward application of the techniques of quantum fields in curved spacetime (Birrell & Davies 1984), the precise calculation involves a level of technical detail beyond the scope of this work. Here we therefore only outline the calculation schematially and refer the reader to one of the many good pedagogical references [e.g., Lyth & Riotto (1999); Liddle & Lyth (2000); Dodelson (2003); Mukhanov (2005); Weinberg (2008); Baumann & McAllister (2015)] for the technical details.

If the scalar field ϕ or Hubble parameter (which is determined at any point by the scalar-

Black-hole analogy

Black Hole

Quantum excitation
of masless modes
(photons)

Classical

Horizon

Inflationary Universe

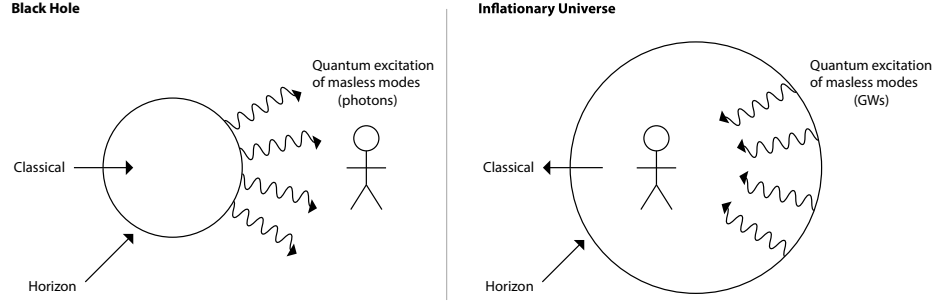Quantum excitation
of masless modes
(GWs)

Classical

Horizon

Figure 2

Left: Hawking radiation from a black-hole event horizon; *Right*: Hawking radiation from an event horizon in an accelerating FRW spacetime. The "classical" arrows indicate the direction of information flow according to classical general relativity.

field value at that point) can vary in time, then they can also vary in space. We thus consider the perturbations to the spacetime metric induced by spatial fluctuations in the scalar field. Since the energy density is determined by ϕ, fluctuations in ϕ will induce fluctuations in the energy density which will then induce fluctuations in the spacetime metric. Although the most general metric perturbation has ten components, four are unphysical gauge modes. Of the remaining six, two are tensor degrees of freedom and two are vector degrees of freedom, none of which can be sourced by perturbations to the scalar field. It can further be shown (e.g., Mukhanov, Feldman & Brandenberger 1992) that the remaining two scalar degrees of freedom are reduced to one for scalar-field perturbations. In the comoving gauge, $g_{0\mu} = 0$, the spatial components of the metric in a scalar-field-dominated Universe are written, $g_{ij} = a^2(t)\exp\left[2\mathcal{R}(\boldsymbol{x},t)\right]\delta_{ij}$, in terms of the "curvature perturbation" $\mathcal{R}(\boldsymbol{x},t)$. Inserting this metric into the Einstein-Hilbert action, combined with the action for the scalar field, and expanding to quadratic order in the perturbation $\mathcal{R}$, we get

$$S_\mathcal{R} = \int dt \int d^3\boldsymbol{x}\, a^3 \left[(1/2)\dot{v}^2 - (1/2)(\nabla v)^2/a^2\right], \tag{7}$$

in terms of a new field variable $v^2 = 2M_{\mathrm{Pl}}{}^2\epsilon\mathcal{R}^2$. Here $\boldsymbol{x}$ is a comoving coordinate and ∇ is a gradient with respect to $\boldsymbol{x}$. We now Fourier transform the spatial part of v to write,

$$S_\mathcal{R} = \sum_{\boldsymbol{k}} \int dt\, a^3 \left[(1/2)|\dot{v}_{\boldsymbol{k}}|^2 - (1/2)(k/a)^2|v_{\boldsymbol{k}}|^2\right], \tag{8}$$

which we recognize as the sum of actions for an ensemble of uncoupled oscillators, one for each $\boldsymbol{k}$, and each with frequency k/a.

This can be seen, if we begin with a Lagrangian, $L = (1/2)\dot{v}^2 - (1/2)k^2 v^2$, by making the variable substitutions $v = \sqrt{m}x$ and $k^2 = \omega^2 = \kappa/m$. We then obtain the Lagrangian $L = (1/2)m\dot{x}^2 - \kappa x^2$ for a simple harmonic oscillator of displacement x, mass m, spring constant κ, and angular frequency ω. We also know that in both the quantum and classical treatments, the average kinetic and potential energies are equal, and equal to half the total energy. Moreover, in the quantum-mechanical ground state, these are both found to be

$\hbar\omega/2$. It thus follows that the probability density to find the oscillator with amplitude v is Gaussian, with variance $\langle v^2 \rangle = \hbar/(2\omega)$.

Now return to Equation 8. Variation of the action for each Fourier mode $\boldsymbol{k}$ results in an equation of motion,

$$\ddot{v}_{\boldsymbol{k}} + 3H\dot{v}_{\boldsymbol{k}} + (k/a)^2 v_{\boldsymbol{k}} = 0, \tag{9}$$

for the time evolution of each $v_{\boldsymbol{k}}$. This is the equation of motion for a simple harmonic oscillator with a time-dependent frequency k/a (the time dependence arises because of the stretching of the wavelength of a comoving Fourier mode) and a friction term $3H$ that arises from the expansion. Consider the system at some range of times t centered around a time T well before horizon exit ($k/a \gg H$) with a spread of times $|t - T| \ll H^{-1}$. Over this range of times, the cosmic expansion is negligible, as is the friction, and the classical solution is simply sinusoidal. The amplitude of the oscillation, in the ground state, is fixed by the requirement $\langle v^2 \rangle = 1/[2(k/a)]$ expected from our discussion of the quantum simple harmonic oscillator. We thus identify $v_{\boldsymbol{k}}(t) = [2E_k]^{-1/2} e^{-iE_k}$, for $k \gg aH$, as the early-time mode function for the ground state of the oscillator, where we have identified $E_k = k/a$ as the energy and $\hbar = 1$. The complete solution to Equation 9, with this normalization at early times, is

$$v_{\boldsymbol{k}}(t) = \frac{H}{(2k^3)^{1/2}} \left(i + \frac{k}{aH} \right) e^{-ik/aH}. \tag{10}$$

We see that at late times, after horizon crossing ($k \ll aH$), the solution approaches $|v_{\boldsymbol{k}}|^2 \rightarrow H^2/(2k^3)$. From this we infer that the inflationary expansion converts subhorizon quantum fluctuations in the curvature to classical superhorizon curvature perturbations. These then become the density perturbations seen in the CMB and that seed the growth of large-scale structure in the later Universe. We moreover see that the primordial curvature perturbation is a realization of a random field in which each Fourier amplitude $\mathcal{R}_{\boldsymbol{k}}$ is selected from a Gaussian distribution with variance, $\langle |\mathcal{R}_{\boldsymbol{k}}|^2 \rangle = H^2/(4M_{\mathrm{Pl}}{}^2 \epsilon k^3)$. We then define the curvature power spectrum,

$$\Delta_{\mathcal{R}}^2(k) \equiv \frac{k^3}{2\pi^2} \langle |\mathcal{R}|^2 \rangle = \frac{1}{8\pi^2} \frac{H^2}{M_{\mathrm{Pl}}{}^2 \epsilon} \simeq \frac{1}{24\pi^2} \frac{V}{M_{\mathrm{Pl}}{}^4 \epsilon}, \tag{11}$$

the contribution per logarithmic interval in k to the real-space curvature variance $\langle \mathcal{R}^2 \rangle = \int d\ln k \Delta_{\mathcal{R}}^2(k)$ (the last term is based on the relation $H^2 \propto V$, from the Friedmann equation, which is valid during slow-roll inflation). From current constraints, $\Delta_{\mathcal{R}}^2 \simeq 2.2 \times 10^{-9}$ [now measured to $\lesssim 1\%$ at 2σ (Ade et al. 2015c)], we infer an upper limit $V^{1/4} \leq 6.6 \times 10^{16} \epsilon^{1/4}$ GeV to the energy scale of inflation. If we assume $\epsilon \lesssim 0.1$, then this is $V^{1/4} \lesssim 3.7 \times 10^{16}$ GeV.

2.2.1. Spectral index for primordial density perturbations. The spectral index $n_s(k)$ for the matter power spectrum is determined by the logarithmic derivative of the power spectrum with respect to wavenumber through,

$$n_s(k) - 1 \equiv \frac{d\ln \Delta_{\mathcal{R}}^2(k)}{d\ln k}. \tag{12}$$

The scale factor a varies much more rapidly than H during inflation, and we evaluate the power-spectrum amplitude at $k = aH$. Therefore, $d\ln k = dk/k \simeq da/a = (\dot{a}/a)dt = H\,dt$. From this, and using $\Delta_{\mathcal{R}}^2(k) \propto H^2/\epsilon$, we infer $n_s - 1 = 2\eta - 6\epsilon$ in terms of the slow-roll parameters ϵ and η defined above. A spectrum with $n_s = 1$, the "Peebles-Harrison-Zelddovich"

spectrum (Peebles & Yu 1970; Harrison 1970; Zeldovich 1970), was postulated well before the advent of inflation simply because this power-law index keeps the perturbation amplitude small on large scales (to preserve the large-scale homogeneity of the Universe) and on small scales (to preserve the sucesses of big-bang nucleosynthesis). Inflation then provided a physical mechanism for generating perturbations with $n_s \simeq 1$. If inflation is at work, though, then some *departure* from $n_s = 1$ is to be expected. In single-field slow-roll inflationary models, $n_s - 1$ can be either positive (in which case the spectrum is said to be "blue") or negative (a "red" spectrum). Planck data now indicate $n_s = 0.968 \pm 0.006$, a $\gtrsim 5\sigma$ discrepancy with $n_s = 1$ (Ade et al. 2014e, 2015c), confirming earlier indications (Komatsu et al. 2009; Calabrese et al. 2013). The finding $n_s \neq 1$ thus supports the notion of inflation. If interpreted within the context of slow-roll inflation, it places very important new constraints to the slope and curvature of the inflaton potential by constraining $6\epsilon - 2\eta = 0.032 \pm 0.006$.

Note also that the power-law index is expected to run with scale (Kosowsky & Turner 1995); i.e., the primordial power spectrum is not a pure power law. In particular, $dn/d \ln k = -16\epsilon\eta + 24\epsilon^2 + \xi^2$, where $\xi^2 \equiv (m_{\mathrm{Pl}}^4/64\pi^2)(V'V'''/V^2)$. Current constraints are consistent with the small value for this running expected if $\epsilon, \eta \lesssim 0.1$ (Ade et al. 2015c).

2.3. Gravitational waves (tensor metric perturbations)

Maxwell's equations in the absence of sources result in a wave equation for the electromagnetic fields. The propagating solutions to these equations are electromagnetic waves, which come with two different linear polarizations. The quanta of these waves are photons. Likewise, the sourceless Einstein's equations for the spacetime metric imply propagating gravitational waves that come in two linear polarizations, denoted + and ×; the quanta of these gravitational waves are gravitons.

Gravitational waves are waves in the transverse ($\partial^i h_{ij}$) and traceless (h^i_i) components of the metric perturbation, defined in the FRW Universe in terms of the spatial components of the metric, by $g_{ij} = a^2(\delta_{ij} + 2h_{ij})$. The Einstein-Hilbert action for the metric, expanded to quadratic order in h_{ij}, is

$$S_h = \frac{1}{4} \int dt \int d^3\boldsymbol{x}\, a^3 M_{\mathrm{Pl}}^2 \left[(1/2) \left(\dot{h}_{ij} \right)^2 - \frac{1}{2a^2} \left(\partial_k h_{ij} \right)^2 \right]. \qquad (13)$$

When written in terms of Fourier modes and in terms of the two gravitational-wave polarizations, of amplitudes h_+ and $h_\times$, this becomes,

$$S_{\mathcal{R}} = \sum_{p=+,\times} \sum_{\boldsymbol{k}} \int dt\, a^3 \left[(1/2)|\dot{v}_{p,\boldsymbol{k}}|^2 - (1/2)(k/a)^2|v_{p,\boldsymbol{k}}|^2 \right], \qquad (14)$$

with $v_p = (M_{\mathrm{Pl}}/2)h_p$. Equation 14 is identical to Equation 8, apart from the sum over polarizations. In other words, each Fourier mode and polarization state of the gravitational wave has an amplitude that behaves like that of a simple harmonic oscillator. Following the same reasoning that led to Equation 11, we find a gravitational-wave power spectrum (after summing over the two polarizations),

$$\Delta_h^2(k) \equiv 2\frac{k^3}{2\pi^2} \langle |h_{p,\boldsymbol{k}}|^2 \rangle = \frac{2}{\pi^2} \frac{H^2}{M_{\mathrm{Pl}}^2}. \qquad (15)$$

Given that $H^2 \propto V$ during inflation, the gravitational-wave amplitude is thus determined entirely by the energy density of the Universe during inflation.

A worked example: Power-law potentials. Here we illustrate the evaluation of the "inflationary observables"—the scalar and tensor power-spectrum amplitudes and their spectral indexes—for a class of inflationary models described by power-law potentials (Linde 1983). We thus take the inflaton potential to be $V(\phi) = (1/2)m^{4-\alpha}\phi^{\alpha}$, where m is a parameter with dimensions of mass or energy, and α is the power-law index. Using the formulas derived in Section 2, the number of e-foldings of inflation between the time that the field takes the value ϕ and the time its value is ϕ_{end} at the end of inflation (when $\epsilon(\phi) \simeq 1$) is $N \simeq (\phi^2 - \phi_{\text{end}}^2)/(2\alpha M_{\text{Pl}}^2)$. The slow-roll parameters are then given in terms of N by $\epsilon = \alpha/(4N)$ and $\eta = (\alpha - 1)/(2N)$. We also have the scalar spectral index $n_s - 1 = -(2 + \alpha)/(2N)$ and $r = 4\alpha/N$. From the value $n_s \simeq 0.968$ from Planck, we infer, for power-law potentials, $N = 62.5\,[1 + (\alpha - 2)/4][(1 - n_s)/0.032]^{-1}$, $\epsilon \simeq 0.008\,(\alpha/2)[1 + (\alpha - 2)/4]^{-1}[(n_s - 1)/0.032]$, and $r \simeq 0.13(\alpha/2)[1 + (\alpha - 2)/4]^{-1}[(n_s - 1)/0.032]$. Using $\phi_{\text{end}}^2 \simeq \alpha^2 M_{\text{Pl}}^2/2$ (from $\epsilon(\phi_{\text{end}}) \simeq 1$), we infer that the energy density at the end of inflation is $V(\phi_{\text{end}}) = m^{4-\alpha}(\alpha M_{\text{Pl}}/\sqrt{2})^{\alpha}/2$. We also infer that the inflaton must traverse a distance $\Delta\phi \gtrsim 16\,(\alpha/2)^{1/2}[1 + (\alpha - 2)/4]^{1/2}[(1 - n_s)/0.032]^{-1/2}\,M_{\text{Pl}}$ during inflation.

The gravitational-wave amplitude is often reported as a tensor-to-scalar ratio,

$$r \equiv \frac{\Delta_h^2}{\Delta_{\mathcal{R}}^2} = 16\epsilon \simeq 0.1 \left(\frac{V}{[2 \times 10^{16}\,\text{GeV}]^4}\right), \qquad (16)$$

where the measured value of $\Delta_{\mathcal{R}}^2$ was used in the last step. The current bound $r \lesssim 0.1$ (Ade et al. 2015a,d) thus provides a slightly stronger constraint to the energy density than the bound from measurement of the scalar amplitude.

As with density perturbations, the gravitational-wave power spectrum is k independent only to the extent that the Hubble parameter H is constant during inflation. Most generally, the inflaton ϕ rolls down the potential $V(\phi)$, and so H decreases as inflation proceeds. There is thus a tensor spectral index,

$$n_t = \frac{d\ln\Delta_h^2(k)}{d\ln k} = -2\epsilon. \qquad (17)$$

which is required to be negative in single-field slow-roll inflation; i.e., gravitational waves are said to have a "red" spectrum. This arises because the energy density during inflation is monotonically decreasing with time.

2.3.1. How big is r?. Given the considerable effort required to seek inflationary gravitational waves, it is important to ask how big the inflationary gravitational wave (IGW) amplitude r is expected to be. Although there are indeed reasonable models that allow for almost arbitrarily small r (as we will illustrate below), there are a variety of arguments that suggest a value $r \gtrsim 10^{-3}$, accessible experimentally within the next 5–10 years.

Within the context of SFSR inflation, the value of r is given once a potential $V(\phi)$ is specified. As Equation 16 indicates, the gravitational-wave amplitude is fixed by the energy density V during inflation (Starobinsky 1979; Rubakov, Sazhin & Veryaskin 1982; Fabbri & Pollock 1983; Abbott & Wise 1984). Originally, the inflaton was thought to have something to do with a Higgs field associated with grand unification. If so, then

a value $V^{1/4} \sim 10^{16}$ GeV (the grand unification energy scale in supersymmetric theories (Dimopoulos, Raby & Wilczek 1981)) was to to be expected, leading to a gravitational-wave amplitude in the ballpark of $r \sim 0.01 - 0.1$. In the years since then there have been a plethora of ideas that identified the inflaton with new physics associated with Peccei-Quinn symmetry breaking (Turner & Wilczek 1991), supersymmetry breaking (Kachru et al. 2003), electroweak-symmetry breaking (Knox & Turner 1993), and a number of other ideas for new physics at energy scales well below that of grand unification. In these models, r is predicted to be far smaller—e.g., as small as $r \sim 10^{-52}$ if the energy scale of inflation is $V^{1/4} \sim$TeV, as may occur if the inflaton has something to do with electroweak symmetry breaking. Thus, until recently, the question of whether the gravitational-wave signal was strong enough to be detected boiled down, in the minds of many theorists, to whether inflation had to do with grand unification.

With empirical evidence in the past few years indicating that $n_s \neq 1$, the thinking on the magnitude of r has shifted. The reasoning, which can be presented in several ways, suggests a value $r \gtrsim 0.001$, although the arguments are never fully conclusive. One argument is based simply upon the relations $n_s - 1 = 2\eta - 6\epsilon$ and $r = 16\epsilon$. If $\eta \sim \epsilon$, then $n_s \simeq 0.968$ implies $\epsilon \sim 0.01$. In this case a value $r \sim 0.1$ is to be expected. If for some reason $\eta \ll \epsilon$, then the 3σ limit $1 - n_s \gtrsim 0.014$ implies $r \gtrsim 0.037$.

There are then lower limits to r that can be obtained within the context of any particular class of inflaton potentials. For example, for the power-law potentials considered above, $1 - n_s \gtrsim 0.014$ implies $r \gtrsim 0.057(\alpha/2)[1 + (\alpha - 2)/4]^{-1}$. For $\alpha = 1$ and $\alpha = 2/3$ [two values that arise in axion-monodromy models of inflation (McAllister, Silverstein & Westphal 2010; Silverstein & Westphal 2008)], the limit evaluates to $r \gtrsim 0.038$ and $r \gtrsim 0.028$, respectively.

Power-law potentials constitute just one of a number of families of inflaton potentials that is far too big to review here. We thus instead just provide a few illustrative examples. Natural inflation (Adams et al. 1993; Freese & Kinney 2015) involves a potential $V(\phi) \propto 1 - \cos(\phi/v)$, where v is a parameter. The analytic relations are not as simple as those for power-law relations; still, one finds $r \gtrsim 0.04$ for the 3σ upper limit $1 - n_s \lesssim 0.05$ (Munoz & Kamionkowski 2015). Inflation with a Higgs-like potential, $V(\phi) \propto (\phi^2 - v^2)^2$, where v is a parameter (Kaplan & Weiner 2004), requires $r \gtrsim 0.03$ for $1 - n_s \lesssim 0.05$ (Munoz & Kamionkowski 2015). One can consider a scenario where $\epsilon \ll \eta$, in which case r could be far smaller than in the hitherto considered example. The unusually small slope V' this scenario requires can be arranged if the inflaton is near a local maximum of $V(\phi)$. Given that V' changes as the inflaton rolls away from the maximum, this scenario requires some tuning, and simple implementations of this idea (for example, in Higgs-like inflation, where the field begins near a local maximum of the potential) still result in values $r \gtrsim 0.01$. Alternatively, a low value of r can be generated by inflection-point inflation (Itzhaki & Kovetz 2007), wherein the inflaton happens to occupy a point in a potential where both V' and V'' are very small.

Other small-r potentials arise from inflation models based on alternative gravity. For example, Starobinsky's R^2 model (Starobinsky 1980; Mukhanov & Chibisov 1981; Ellis, Nanopoulos & Olive 2013; Buchmuller, Domcke & Kamada 2013), in which the action for gravity contains a term quadratic in the Ricci scalar R in addition to the linear term that appears in the usual Einstein-Hilbert action. The resulting dynamics can be mapped onto those of SFSR inflation with a fairly exotic-looking potential. This model predicts $r = 3(n_s - 1)^2$ which yields $r \simeq 0.003$ for the Planck central value of $n_s \simeq 0.968$ and $r \gtrsim 6 \times 10^{-4}$ for the 3σ limit $1 - n_s \gtrsim 0.014$. The same prediction holds for the "Higgs

Constraints from n_s:

ϕ^2 Inflation:

best-fit r	3σ bound
0.13	0.057

Monodromy ϕ:

best-fit r	3σ bound
0.087	0.038

Monodromy $\phi^{2/3}$:

best-fit r	3σ bound
0.065	0.028

R^2 Inflation:

best-fit r	3σ bound
0.003	6×10^{-4}

Natural Inflation:

3σ bound
0.04

Higgs-like Potential:
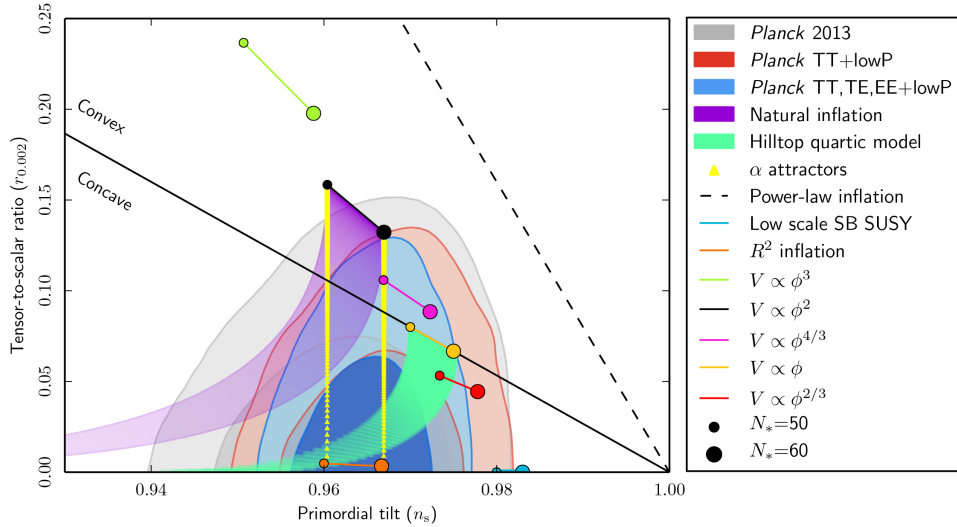
3σ bound
0.03

Figure 3

The current constraints, from the Planck Collaboration (Ade et al. 2015d), to the scalar spectral index n_s and tensor-to-scalar ratio r. Shown are predictions for a variety of slow-roll models. The "concave" and "convex" refer to the sign of the second derivative V'' of the inflaton potential.

Inflation" model (Bezrukov & Shaposhnikov 2008). Several potentials [e.g., a Coleman-Weinberg potential (Coleman & Weinberg 1973) and others (Kinney & Mahanthappa 1996)] considered prior to the discovery $n_s \simeq 1$ to illustrate that r could be virtually arbitrarily small predict, with current constraints to n_s, values $r \gtrsim 0.01$ (Kinney 2015). Although this does not rule out the possibility $r \ll 0.001$ in SFSR, it indicates the increased pressure on low-r SFSR models provided by the measurement of n_s.

The estimates done here (and listed in the sidebar), which have assumed a specific 3σ error range for n_s, actually simplify a bit the actual current constraints to the model parameter space. As shown in **Figure 3**, experiments provide joint constraints to the n_s-r parameter space (Ade et al. 2015d), and so the constraints to models are generally stronger than what we have assumed here.

Large-field versus small-field models. There is an interesting model-independent argument that suggests a qualitative difference between SFSR models with $r \gtrsim 10^{-3}$ and those with $r \lesssim 10^{-3}$ (Turner 1993; Lyth 1997). This "Lyth bound" follows from Equation 4 and the relation $r \simeq 16\,\epsilon$. If ϵ is roughly constant during inflation, then we infer that the distance $\Delta\phi$ traversed by the inflaton during inflation is

$$\frac{\Delta\phi}{M_{\mathrm{Pl}}} \gtrsim \sqrt{\frac{r}{8}}N \simeq \left(\frac{r}{10^{-3}}\right)^{1/2}\left(\frac{N}{10}\right), \tag{18}$$

where the inequality comes from the fact that there may be many more e-folds of inflation that precede those required for observations within our horizon. Thus, $r \gtrsim 10^{-3}$ requires $\Delta\phi > M_{\mathrm{Pl}}$, a "large-field" model of inflation, while $r \lesssim 10^{-3}$ allows for $\Delta\phi \lesssim M_{\mathrm{Pl}}$ (a "small-field" model).

While the construction of any workable SFSR potential requires what virtually any particle theorist would consider fine tuning (in order to sustain slow-roll for the required number of e-folds), large-field models pose an even greater challenge for model builders. Suppose we Taylor expand the potential about its minimum (assumed to be $V = 0$),

$$V(\phi) = \frac{1}{2}m^2\phi^2 + \phi^2 \sum_{p=1}^{\infty} \lambda_p \left(\frac{\phi}{M_{\rm Pl}}\right)^p. \tag{19}$$

We can always choose the coefficients λ_p so that $\epsilon, \eta \ll 1$ at some particular value of ϕ. These coefficients, though, are expected to receive contributions $\Delta\lambda_p(\phi)$ from quantum corrections that are themselves functions of ϕ. These corrections are then expected to vary by order unity over distances $\Delta\phi \gtrsim M_{\rm Pl}$. It is thus difficult to see how a generic potential can preserve $\epsilon, \eta \ll 1$ over an inflaton displacement $\Delta\phi \gtrsim M_{\rm Pl}$. This problem is averted if there are symmetries that set some of these coefficients or the corrections to zero, and a theoretical industry has developed to construct string-inspired models that preserve $\epsilon, \eta \ll 1$ with large field excursions (Baumann & McAllister 2009, 2015). It should also be emphasized that the boundary between small-field and large-field models is blurry (Itzhaki & Kovetz 2009). Still, an experiment with a detection sensitivity of $r \sim 10^{-3}$ would provide a fairly definitive statement about the validity (or otherwise) of large-field SFSR models.

Beyond-SFSR inflation. As will be discussed below, the predictions of SFSR inflation are in exquisite agreement with a wealth of precise measurements, and there are no experimental nor observational results that drive us to introduce any new physics beyond that found in SFSR inflation. Still, SFSR inflation should be viewed as no more than a working or toy model, and a vast theoretical literature that explores ideas for beyond-SFSR inflation has evolved. In many of these, the connections between n_s and r found in SFSR models are either revised or lost. For example, in models with modifications to the kinetic term in the inflaton Lagrangian (Alishahiha, Silverstein & Tong 2004; Armendariz-Picon, Damour & Mukhanov 1999), the GW amplitude can be suppressed by the speed of sound c_s, for inflaton perturbations, which may be very small. Even so, the remarkable success of the simplest SFSR model, along with current constraints to n_s, make a compelling case, many theorists would agree, for a measurement sensitive to $r \sim 0.001$.

In this context, it is worth mentioning that an important property of simple models of inflation—that a measurement of the amplitude of tensor modes is in one-to-one correspondence with the energy scale of inflation—has been augmented in models involving spectator fields that are excited from the vacuum during inflation and possibly enhance the tensor fluctuation spectrum (Senatore, Silverstein & Zaldarriaga 2014; Cook & Sorbo 2012; Barnaby et al. 2012). However, these models appear to require complex setups (Carney et al. 2012; Kleban, Mirbabayi & Porrati 2015), and tend to produce tension with constraints on scalar fluctuations and non-gaussianity (Mirbabayi et al. 2015; Özsoy, Sinha & Watson 2015).

3. From gravitational waves to the CMB

We now show how gravitational waves induce temperature fluctuations and polarization in the cosmic microwave background. Following the pioneering work of Polnarev (1986) [see also Cabella & Kamionkowski (2004)], we first derive the angular distribution of photon intensities in the presence of a gravitational wave (GW). Suppose that the Universe is filled

with photons that do not scatter. In this case, the photon energies are affected only by the form of the metric. Consider a single monochromatic plane-wave gravitational wave, which appears as a tensor perturbation to the FRW metric,

$$ds^2 = a^2(\eta) \left[d\eta^2 - dx^2(1 + h_+) + dy^2(1 - h_+) + dz^2 \right],$$ (20)

where η is the conformal time and

$$h_+(\boldsymbol{x}, \eta) \simeq h(\eta) e^{ik\eta} e^{-ikz},$$ (21)

describes a plane wave propagating in the $\hat{z}$ direction. This is a linearly-polarized gravitational wave with "+" (rather than "×") polarization. Here $h(\eta)$ is the amplitude; at early times when $k\eta \lesssim 1$, $h(\eta) \simeq$ const, but then $h(\eta)$ redshifts away when $k\eta \gtrsim 1$. If we construct the Einstein tensor $G_{\mu\nu}$ from the metric, Equation 20, then the vacuum Einstein equation $G_{\mu\nu} = 0$ leads to the wave equation for $h_+(\boldsymbol{x}, t)$. The "$\simeq$" sign appears in Equation 21 because the gravitational waves do not propagate in a vacuum but rather in a Universe filled with a cosmic fluid. The anisotropic stress of this fluid (to which the neutrino background contributes after neutrinos decouple) modifies slightly the time evolution, a calculable $\sim 10\%$ correction to Equation 21 (Weinberg 2004; Pritchard & Kamionkowski 2005; Dicus & Repko 2005).

Photons that propagate freely through this spacetime experience a frequency shift $d\nu$ during an expansion interval $d\eta$ determined by the geodesic equation, which in this spacetime takes the form,

$$\frac{1}{\nu} \frac{d\nu}{d\eta} = -\frac{1}{2}(1 - \mu^2) \cos 2\phi \, e^{-ikz} \frac{d}{d\eta}(he^{ik\eta}),$$ (22)

where μ is the cosine of the angle that the photon trajectory makes with the z axis, and ϕ is the azimuthal angle of the photon's trajectory. This redshifting is polarization-independent, but polarization is then induced by Thomson scattering of this anisotropic radiation field. To account for the polarization, we must follow the time evolution of four distribution functions (DFs) $f_s(\boldsymbol{x}, \boldsymbol{q}; \eta)$ (Crittenden 1993; Crittenden, Davis & Steinhardt 1993; Crittenden, Coulson & Turok 1995), where $\boldsymbol{q}$ is the photon momentum, for $s = I$, Q, U, and V, the four Stokes parameters required to specify the polarization. The original (unperturbed) distribution function is $\bar{f}_I(\boldsymbol{q}, \boldsymbol{x}; \eta) = \left[e^{h\nu/k_B T(\eta)} - 1 \right]^{-1}$, where k_B is the Boltzmann constant and $T(\eta)$ the unperturbed CMB temperature at conformal time η, and $\bar{f}_Q = \bar{f}_U = \bar{f}_V = 0$. We then define perturbations $\Delta_s e^{i\boldsymbol{k}\cdot\boldsymbol{x}} = 4\delta f_s / (\partial \bar{f} / \partial \ln T)$, suppressing an index $\boldsymbol{k}$ for notational economy. Thomson scattering induces no ciruclar polarization, so $\Delta_V = 0$ at all times. Since the gravitational redshift and Thomson scattering are frequency independent, the evolution of the distribution function is the same for all frequencies. Since the $e^{i\boldsymbol{k}\cdot\boldsymbol{x}}$ spatial dependence of the DFs is separated out in the definition of Δ_s, the perturbed DFs are functions $\Delta_s(\hat{q}; \eta)$ only of the direction $\hat{q}$ of the photon and the conformal time η. Finally, if we define perturbation variables $\tilde{\Delta}_s$ by

$$\Delta_I = \tilde{\Delta}_I (1 - \mu)^2 \cos 2\phi, \qquad \Delta_Q = \tilde{\Delta}_Q (1 + \mu)^2 \cos 2\phi, \qquad \Delta_U = \tilde{\Delta}_U 2\mu \sin 2\phi, \quad (23)$$

the new variables $\tilde{\Delta}_s(\mu; \eta)$ are now functions only of μ and there is a relation $\tilde{\Delta}_Q = -\tilde{\Delta}_U$ for the gravitational wave, a consequence of the fact that the orientation of the photon polarization is fixed by the direction of the photon with respect to the GW polarization

tensor. As a result, the Boltzmann equations for the distribution functions reduce to two equations (Crittenden, Davis & Steinhardt 1993; Kosowsky 1996; Ma & Bertschinger 1995),

$$\dot{\tilde{\Delta}}_I + ik\mu\tilde{\Delta}_T = -\dot{h} - \dot{\kappa}\left[\tilde{\Delta}_T - \Psi\right], \qquad \dot{\tilde{\Delta}}_Q + ik\mu\tilde{\Delta}_Q = -\dot{\kappa}\left[\Delta_P + \Psi\right], \qquad (24)$$

where the dot denotes derivative with respect to conformal time. Here, the variable

$$\Psi \equiv \left[\frac{1}{10}\tilde{\Delta}_{I0} + \frac{1}{7}\tilde{\Delta}_{T2} + \frac{3}{70}\tilde{\Delta}_{T4} - \frac{3}{5}\tilde{\Delta}_{Q0} + \frac{6}{7}\tilde{\Delta}_{Q2} - \frac{3}{70}\tilde{\Delta}_{Q4}\right], \qquad (25)$$

is given in terms of the Legendre moments $\tilde{\Delta}_{I\ell}(\eta) = (1/2)\int_{-1}^{1} d\mu\, \tilde{\Delta}_I(\mu;\eta)P_\ell(\mu)$ (and similarly for $\tilde{\Delta}_{Q\ell}$), where $P_\ell(\mu)$ is a Legendre polynomial. The quantity $\dot{\kappa}\delta = (d\kappa/d\eta)d\eta$ is the contribution to the Thomson optical depth in the conformal-time interval $d\eta$.

Equations 24 and 25 look complicated but describe relatively simple physics. The left-hand sides of Equation 24 are simply the Lagrangian time derivatives for a Fourier mode of wavenumber k. The $\dot{h}$ in the first equation accounts for the intensity variation (described above) induced by the gravitational redshift; its absence from the second equation is because the gravitational redshift is polarization-independent. As the presence of the differential Thomson optical depth $\dot{\kappa}$ suggests, the terms on the right-hand sides of Equations 24 involving Ψ, $\tilde{\Delta}_I$, and $\tilde{\Delta}_P$ account for Thomson scattering. They are derived using the dependence $d\sigma_T/d\Omega \propto (\hat{\epsilon}_i \cdot \hat{\epsilon}_f)^2$ of the Thomson differential cross section on the polarization vectors $\hat{\epsilon}_i$ and $\hat{\epsilon}_f$ of the initial- and final-state photons. This dependence also explains why a quadrupolar anisotropy in the incoming radiation is required in order to generate the linear polarization signal, as was first realized in Rees (1968).

Still, Equations 24) and 25 constitute a set of coupled partial integro-differential equations. In practice, they are solved numerically by expanding $\tilde{\Delta}_I$ and $\tilde{\Delta}_Q$ in terms of their Legendre moments and thus recasting the equations as an infinite set of coupled Boltzmann equations for $\tilde{\Delta}_{I\ell}(\eta)$ and $\tilde{\Delta}_{Q\ell}(\eta)$ (Crittenden, Davis & Steinhardt 1993; Kosowsky 1996). They are then solved numerically by integrating from some early time and truncating the hierarchy at some sufficiently high ℓ.

Later we will return to these equations, but for now we show in **Figure 4(b)** the resulting CMB temperature-polarization pattern induced by one gravitational wave propagating in the $\hat{z}$ direction (Caldwell, Kamionkowski & Wadley 1999). The quadrupolar variation (i.e., the $\cos 2\phi$ dependence) of the temperature-polarization pattern can be seen as one travels along a curve of constant latitude, and the wavelike pattern can be seen as one moves along a line of constant longitude. It can be seen that as we move along the line of constant longitude, there are variations in Q, the component of the polarization perpendicular/parallel to those constant-longitude lines. It can also be seen, however, that there are variations in U, the component of the polarization $45°$ with respect to constant-longitude lines. This, as we will see below, is a signature of the B mode in the CMB polarization pattern induced by the gravitational wave. This is to be contrasted with the polarization pattern, shown in **Figure 4(a)**, for a single Fourier mode of the density field. In this case, there is no variation along lines of constant latitude, and there is only variation in Q, and thus no B mode, as we will see.

Still, inflation predicts not a single gravitational wave of given wavevector and polarization, but rather a statistically isotropic stochastic background of gravitational waves. The next step is thus to understand how to represent the polarization pattern induced by this stochastic background.
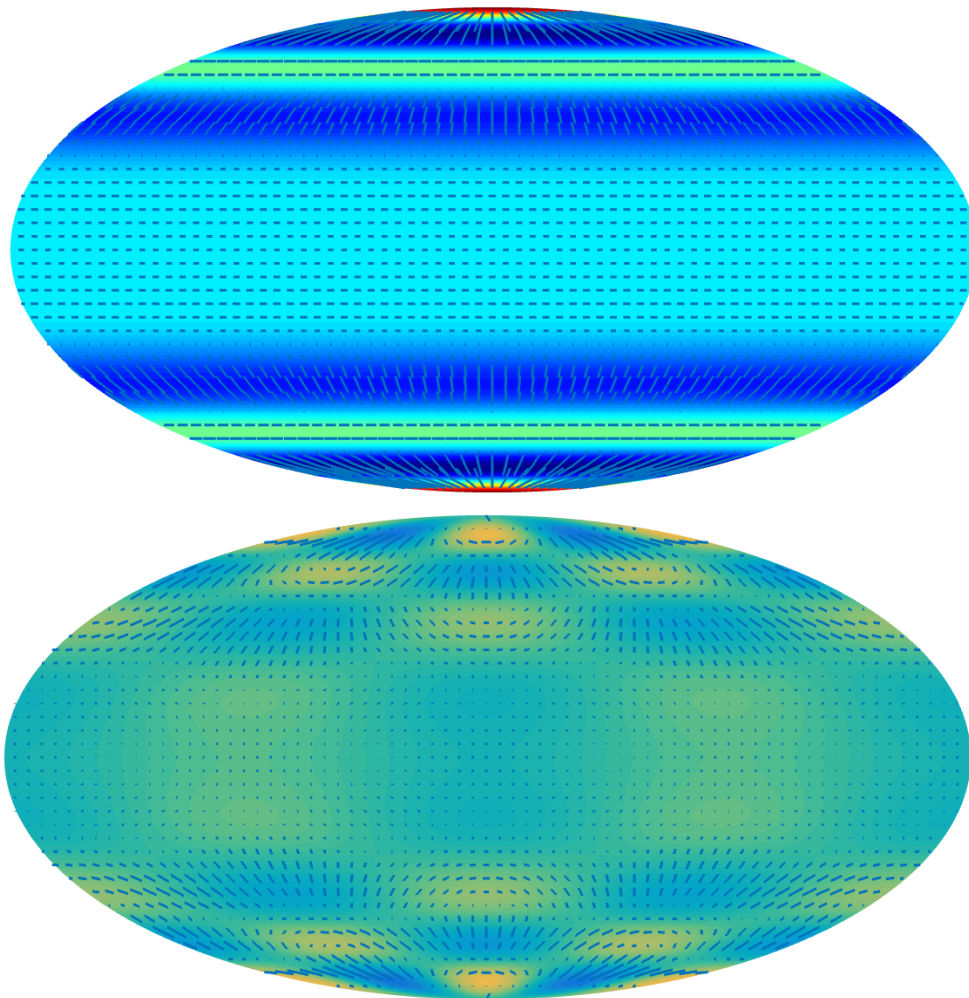
Figure 4

Top: The CMB temperature-polarization pattern induced by one Fourier mode of the density field (i.e., a scalar metric perturbation). The polarization pattern varies along a direction parallel/perpendicular to lines of constant longitude that align with the direction of the wave. The induced polarization pattern is thus a pure E mode. *Bottom:* The same for a single gravitational wave (i.e., a single Fourier mode of the tensor field). We see that in this case, there is variation of the polarization not only parallel/perpendicular to lines of constant longitude, but also along directions 45° with respect to these lines. There is thus a B mode induced.

4. Harmonic analysis for CMB polarization

We therefore turn to the mathematical description of the polarization. Stokes parameters Q and U are coordinate-dependent quantities. Suppose that they are measured with respect to some x-y axes and that we then consider some other x'-y' axes rotated by an angle α with respect to the x-y axes. Under this rotation, the Stokes parameters (Q, U) transform

as components of a symmetric trace-free (STF) 2×2 tensor,

$$\begin{pmatrix} Q & U \\ U & -Q \end{pmatrix} \Rightarrow \begin{pmatrix} \cos\alpha & \sin\alpha \\ -\sin\alpha & \cos\alpha \end{pmatrix} \begin{pmatrix} Q & U \\ U & -Q \end{pmatrix} \begin{pmatrix} \cos\alpha & -\sin\alpha \\ \sin\alpha & \cos\alpha \end{pmatrix}. \tag{26}$$

Alternatively and equivalently, if we represent the polarization by a complex number $P = Q + iU$, then $P \to Pe^{2i\alpha}$ under a rotation of the coordinate axes by an angle α; i.e., the polarization is a spin-2 field.

Anything we say about Stokes parameters Q and U are thus tied to the coordinate system we choose. We will therefore want to find a coordinate-system–independent representation of this tensor field if we are to make statements about physics that are independent of coordinate system. Later, we will do this on the full sky, but we first do the simpler case of a flat sky (which also serves as a good approximation to a small region of the sky).

4.1. Harmonic analysis on a flat sky

Once the polarization, $Q(\boldsymbol{\theta})$ and $U(\boldsymbol{\theta})$, has been measured as a function of position $\boldsymbol{\theta} = (\theta_x, \theta_y)$ on a flat region of sky, we have measured the polarization tensor field,

$$\mathcal{P}_{ab} = \frac{1}{\sqrt{2}} \begin{pmatrix} Q(\boldsymbol{\theta}) & U(\boldsymbol{\theta}) \\ U(\boldsymbol{\theta}) & -Q(\boldsymbol{\theta}) \end{pmatrix}, \tag{27}$$

where the normalization is chosen so that $\mathcal{P}^{ab}\mathcal{P}_{ab} = Q^2 + U^2$ and so that the conventions for the E and B modes defined below agree with those of Seljak & Zaldarriaga (1997) and Zaldarriaga & Seljak (1997) and are identified with the G and C modes of Kamionkowski, Kosowsky & Stebbins (1997a,b) through $a^{\text{G}}_{(\ell m)} = a^{\text{E}}_{\ell m}/\sqrt{2}$ and $a^{\text{C}}_{(\ell m)} = a^{\text{B}}_{\ell m}/\sqrt{2}$.

We now define gradient ("E modes") and curl ("B modes") components of the tensor field that are independent of the orientation of the x-y axes by

$$\nabla^2 E = \partial_a \partial_b \mathcal{P}_{ab}, \qquad \nabla^2 B = \epsilon_{ac} \partial_b \partial_c \mathcal{P}_{ab}, \tag{28}$$

where ϵ_{ab} is the antisymmetric tensor.

Writing,

$$\mathcal{P}_{ab}(\boldsymbol{\theta}) = \int \frac{d^2\boldsymbol{\ell}}{(2\pi)^2} \tilde{\mathcal{P}}_{ab}(\boldsymbol{\ell}) e^{-i\boldsymbol{\ell}\cdot\boldsymbol{\theta}}, \qquad \tilde{\mathcal{P}}_{ab}(\boldsymbol{\ell}) = \int d^2\boldsymbol{\theta} \mathcal{P}_{ab}(\boldsymbol{\theta}) e^{i\boldsymbol{\ell}\cdot\boldsymbol{\theta}}, \tag{29}$$

the Fourier components of $E(\boldsymbol{\theta})$ and $B(\boldsymbol{\theta})$ are

$$\begin{pmatrix} \tilde{E}(\boldsymbol{\ell}) \\ \tilde{B}(\boldsymbol{\ell}) \end{pmatrix} = \frac{1}{\sqrt{2}} \begin{pmatrix} \cos 2\varphi_{\boldsymbol{\ell}} & \sin 2\varphi_{\boldsymbol{\ell}} \\ -\sin 2\varphi_{\boldsymbol{\ell}} & \cos 2\varphi_{\boldsymbol{\ell}} \end{pmatrix} \begin{pmatrix} \tilde{Q}(\boldsymbol{\ell}) \\ \tilde{U}(\boldsymbol{\ell}) \end{pmatrix}, \tag{30}$$

where $\varphi_{\boldsymbol{\ell}}$ is the angle $\boldsymbol{\ell}$ makes with the $\hat{x}$ axis. This relation can be inverted,

$$\begin{pmatrix} \tilde{Q}(\boldsymbol{\ell}) \\ \tilde{U}(\boldsymbol{\ell}) \end{pmatrix} = \sqrt{2} \begin{pmatrix} \cos 2\varphi_{\boldsymbol{\ell}} & -\sin 2\varphi_{\boldsymbol{\ell}} \\ \sin 2\varphi_{\boldsymbol{\ell}} & \cos 2\varphi_{\boldsymbol{\ell}} \end{pmatrix} \begin{pmatrix} E(\boldsymbol{\ell}) \\ B(\boldsymbol{\ell}) \end{pmatrix}. \tag{31}$$

Thus, for a pure B mode in the $\hat{x}$ direction ($\varphi_{\boldsymbol{\ell}} = 0$), we have (as shown in the right panel of **Figure 5**) $\tilde{Q}(\boldsymbol{\ell}) = 0$ and $\tilde{U}(\boldsymbol{\ell}) = \tilde{B}(\boldsymbol{\ell})$. For a pure E mode in the $\hat{x}$ direction, we have (as shown in the left panel of **Figure 5**) $\tilde{Q}(\boldsymbol{\ell}) = \tilde{E}(\boldsymbol{\ell})$ and $\tilde{U}(\boldsymbol{\ell}) = 0$. Thus, *in an E mode,*
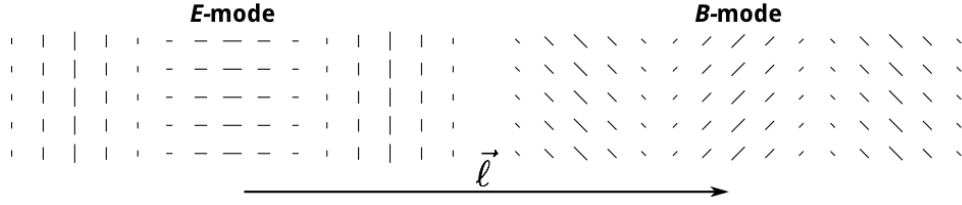
E-mode   **B-mode**

Figure 5

Shown are the polarization pattern associated with a single E mode (left) and a single B mode (right) with a horizontal wavevector $\boldsymbol{\ell}$. The E mode features a variation of the polarization along directions parallel/perpendicular to the direction of $\boldsymbol{\ell}$ (Stokes parameter Q in a coordinate system aligned with $\boldsymbol{\ell}$), while in the B mode the variation in the polarization is along directions $45°$ with respect to $\boldsymbol{\ell}$ (Stokes parameter U in coordinates aligned with $\boldsymbol{\ell}$). (From C. Bischoff.)

the polarization varies parallel/perpendicular to the direction of the Fourier mode, while for a B mode the polarization varies along directions $45°$ with respect to the direction of the Fourier mode.

Since the combined temperature/polarization map is described by three sets, $\tilde{T}(\boldsymbol{\ell})$, $\tilde{E}(\boldsymbol{\ell})$, and $\tilde{B}(\boldsymbol{\ell})$, of Fourier components, the two-point statistics of the temperature/polarization field are determined by a total of six power spectra, $C_\ell^{X_1, X_2}$, defined by

$$\left\langle \tilde{X}_1(\boldsymbol{\ell}) \tilde{X}_2(\boldsymbol{\ell}') \right\rangle = (2\pi)^2 \delta(\boldsymbol{\ell} + \boldsymbol{\ell}') C_\ell^{X_1 X_2}, \tag{32}$$

where $X_1, X_2 = \{T, E, B\}$. Here the angle brackets denote an average over all realizations of the temperature map.

Now suppose we have a given temperature/polarization map and then consider a parity inversion; e.g., a reflection about the x-axis. Then

$$\theta_y \to -\theta_y, \quad Q \to Q, \quad U \to -U, \quad \ell_x \to \ell_x, \quad \ell_y \to -\ell_y. \tag{33}$$

Also,

$$\tilde{T}(\boldsymbol{\ell}) \to \tilde{T}(\boldsymbol{\ell}), \quad \tilde{E}(\boldsymbol{\ell}) \to \tilde{E}(\boldsymbol{\ell}), \quad \tilde{B}(\boldsymbol{\ell}) \to -\tilde{B}(\boldsymbol{\ell}). \tag{34}$$

Thus, T and E have the same parity, while B has the opposite parity. If the physics that gives rise to temperature/polarization fluctuations is parity conserving, we then expect $C_\ell^{TB} = C_\ell^{EB} = 0$. In this case, the statistics of the temperature/polarization map are determined entirely by the four power spectra, C_ℓ^{TT}, C_ℓ^{TE}, C_ℓ^{EE}, and C_ℓ^{BB}.

4.2. Harmonic analysis on the full sky

If our maps extend beyond a small region of the sky, we will have to deal with the curvature of the sky. We thus generalize the tensor Fourier analysis that we carried out above for STF 2×2 tensors to tensors that live on the 2-sphere. Our discussion follows Kamionkowski, Kosowsky & Stebbins (1997b); a different but equivalent formalism is presented in Zaldarriaga & Seljak (1997). In the usual spherical polar coordinates θ, ϕ, the sphere has a metric, $g_{ab} = \text{diag}(1, \sin^2 \theta)$. The polarization tensor $\mathcal{P}_{ab}$ must be symmetric $\mathcal{P}_{ab} = \mathcal{P}_{ba}$ and trace-free $g^{ab} \mathcal{P}_{ab} = 0$, from which it follows that,

$$\mathcal{P}_{ab}(\hat{n}) = \frac{1}{\sqrt{2}} \begin{pmatrix} Q(\hat{n}) & U(\hat{n}) \sin\theta \\ U(\hat{n}) \sin\theta & -Q(\hat{n}) \sin^2\theta \end{pmatrix}, \tag{35}$$

where the factors of $\sin\theta$ follow from the fact that the coordinate basis (θ, ϕ) is orthogonal but not orthonormal.

We use a colon (:) to denote a covariant derivative on the surface of the sphere (e.g., $S^a_{:a}$ denotes the divergence of S^a) and a comma to denote a partial derivative [e.g., $S_{,a} = (\partial S/\partial x^\alpha)$]. Appendix A of Kamionkowski, Kosowsky & Stebbins (1997b) reviews the rules of differential geometry on the sphere in the notation we use here.

Any STF 2×2 tensor field on the sphere can be written as the 'gradient', $E_{:ab} - \frac{1}{2}g_{ab}E_c^{:c}$, of some scalar field $E(\theta, \phi)$, plus the 'curl,' $(1/2)\,(B_{:ac}\epsilon^c_b + B_{:bc}\epsilon^c_a)$, of some other scalar field $B(\theta, \phi)$, For comparison, a vector field is analogously decomposed as $V_a = \nabla_a E + \epsilon_{ab}\nabla_b B$. Since any scalar field on the sphere can be expanded in spherical harmonics (e.g. for the temperature),

$$\frac{T(\hat{n})}{T_0} = 1 + \sum_{\ell=1}^{\infty}\sum_{m=-\ell}^{\ell} a_{\ell m}^{\mathrm{T}}\, Y_{\ell m}(\hat{n}), \qquad \text{where} \qquad a_{\ell m}^{\mathrm{T}} = \frac{1}{T_0}\int d\hat{n}\, T(\hat{n})Y_{\ell m}^*(\hat{n}), \qquad (36)$$

it follows that the polarization tensor can be expanded in terms of basis functions that are gradients and curls of spherical harmonics,

$$\mathcal{P}_{ab}(\hat{n}) = T_0 \sum_{\ell=2}^{\infty}\sum_{m=-\ell}^{\ell}\left[a_{\ell m}^{\mathrm{E}}Y_{(\ell m)ab}^{\mathrm{E}}(\hat{n}) + a_{\ell m}^{\mathrm{B}}Y_{(\ell m)ab}^{\mathrm{B}}(\hat{n})\right]. \qquad (37)$$

The expansion coefficients are given by

$$a_{\ell m}^{\mathrm{E}} = \frac{1}{T_0}\int d\hat{n}\mathcal{P}_{ab}(\hat{n})Y_{(\ell m)}^{\mathrm{E}\,ab\,*}(\hat{n}), \qquad\qquad a_{\ell m}^{\mathrm{B}} = \frac{1}{T_0}\int d\hat{n}\,\mathcal{P}_{ab}(\hat{n})Y_{(\ell m)}^{\mathrm{B}\,ab\,*}(\hat{n}), \qquad (38)$$

and

$$Y_{(\ell m)ab}^{\mathrm{E}} = N_\ell\left(Y_{(\ell m):ab} - \frac{1}{2}g_{ab}Y_{(\ell m):c}{}^c\right), \quad Y_{(\ell m)ab}^{\mathrm{B}} = \frac{N_\ell}{2}\left(Y_{(\ell m):ac}\epsilon^c{}_b + Y_{(\ell m):bc}\epsilon^c{}_a\right), \quad (39)$$

constitute a complete orthonormal set of basis functions for the E and B components of the polarization. The quantity, $N_\ell \equiv \sqrt{2(l-2)!/(l+2)!}$, is a normalization factor chosen so that

$$\int d\hat{n}\, Y_{(\ell m)ab}^{\mathrm{X}\,*}(\hat{n})\, Y_{(l'm')}^{\mathrm{X}'\,ab}(\hat{n}) = \delta_{\ell\ell'}\delta_{mm'}, \qquad (40)$$

for XX$'$ =EE, EB, and BB. Also, we can integrate by parts to write alternatively,

$$a_{\ell m}^{\mathrm{E}} = \frac{N_\ell}{T_0}\int d\hat{n}\, Y_{\ell m}^*(\hat{n})\, \mathcal{P}_{ab}{}^{:ab}(\hat{n}), \qquad\qquad a_{\ell m}^{\mathrm{B}} = \frac{N_\ell}{T_0}\int d\hat{n}\, Y_{(\ell m)}^*(\hat{n})\, \mathcal{P}_{ab}{}^{:ac}(\hat{n})\epsilon_c{}^b. \qquad (41)$$

Finally, since T, Q, and U are real, we get $a_{\ell m}^{\mathrm{X}\,*} = (-1)^m a_{\ell,-m}^{\mathrm{X}}$, where X = $\{\mathrm{T}, \mathrm{E}, \mathrm{B}\}$. The temperature/polarization power spectra are now

$$\left\langle a_{\ell m}^{\mathrm{X}\,*} a_{\ell' m'}^{\mathrm{X}'}\right\rangle = C_\ell^{\mathrm{XX}'}\delta_{\ell\ell'}\delta_{mm'}, \qquad (42)$$

for XX$'$ =TT, EE, BB, TE, TB, and EB. The C_ℓ here reduce in the small-angle (large-ℓ) limit with those in Section 4.1 as long as the angles in the flat-sky limit are given in radians.

The $Y_{(\ell m)ab}^{\mathrm{E}}$ and $Y_{(\ell m)ab}^{\mathrm{B}}$ are explicitly given by

$$Y_{(\ell m)ab}^{\mathrm{E}} = \frac{N_\ell}{2}\begin{pmatrix} W_{\ell m} & X_{\ell m}\sin\theta \\ X_{\ell m}\sin\theta & -W_{\ell m}\sin^2\theta \end{pmatrix}, \quad Y_{(\ell m)ab}^{\mathrm{B}} = \frac{N_\ell}{2}\begin{pmatrix} -X_{\ell m} & W_{\ell m}\sin\theta \\ W_{\ell m}\sin\theta & X_{\ell m}\sin^2\theta \end{pmatrix},$$
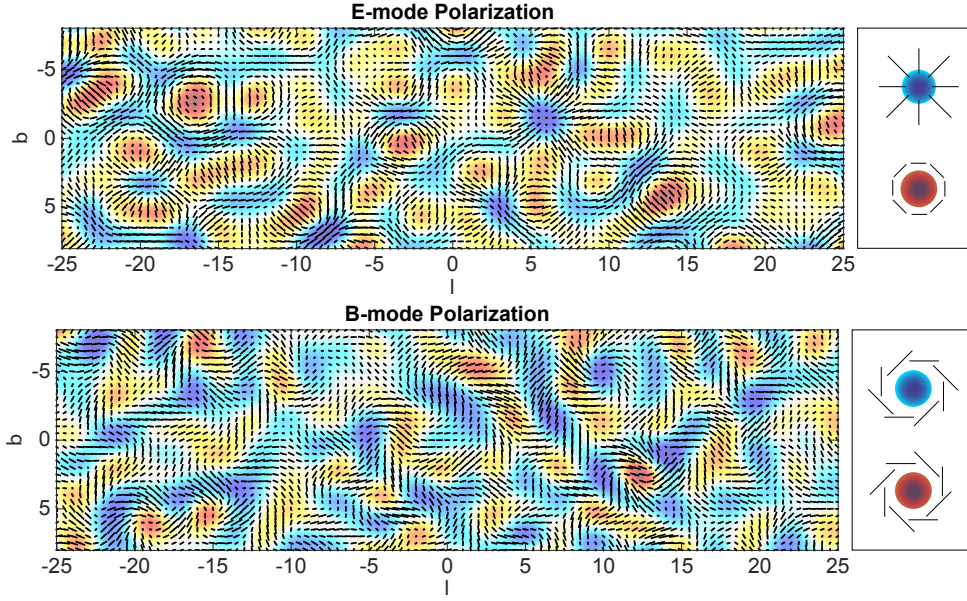$$(43)$$

E-mode Polarization

B-mode Polarization

In the top figure we show a polarization pattern composed only of E modes and in the bottom one composed only of B modes. As indicated on the right, it is seen that around hot spots (red) the polarization pattern of the E mode is tangential and radial around cold spots (blue). The polarization pattern surrounding hot and cold spots of the B mode show a characteristic swirling pattern (with different orientation around hot and cold spots).

where

$$W_{\ell m}(\hat{n}) \pm iX_{\ell m}(\hat{n}) = \sqrt{\frac{(l+2)!}{(l-2)!}} \,_{\pm 2}Y_{\ell m}(\hat{n}), \tag{44}$$

in terms of the spin-2 harmonics $_{\pm 2}Y_{\ell m}$ used in Seljak & Zaldarriaga (1997), Zaldarriaga & Seljak (1997), and Hu & White (1997b). If we replace (Q, U) by $(U, -Q)$, then $\text{E} \to -\text{B}$ and $\text{B} \to \text{E}$. This tells us therefore, that a pure-E polarization pattern becomes a pure-B pattern if we rotate each polarization vector by $45°$, and *vice versa*, as can be also inferred from the flat-sky treatment. Examples of E and B type polarization patterns are shown in **Figure 6**. The parity properties of T, E, and B found in the flat-sky treatment remain valid on the full sky.

5. E and B modes from gravitational waves

We now return to the polarization pattern induced by a single gravitational wave, of + polarization, of wavelength k propagating in the $\hat{z}$ direction. The upshot of Section 3 is that this gravitational wave induces a polarization tensor (Kosowsky 1996),

$$\mathcal{P}^{ab}_{\boldsymbol{k},+}(\theta, \phi) = \frac{T_0}{4\sqrt{2}} \sum_{\ell} (2\ell+1) P_{\ell}(\cos\theta) \tilde{\Delta}_{Q\ell} \begin{pmatrix} (1+\cos^2\theta)\cos 2\phi & 2\cot\theta\sin 2\phi \\ 2\cot\theta\sin 2\phi & -(1+\cos^2\theta)\csc^2\theta\cos 2\phi \end{pmatrix}. \tag{45}$$

If we expand this in tensor spherical harmonics, the resulting coefficients are (Kamionkowski, Kosowsky & Stebbins 1997b; Zaldarriaga & Seljak 1997),

$$a_{\ell m}^{\mathrm{E}\,\boldsymbol{k},+} = \frac{\sqrt{\pi(2\ell+1)}}{4(\delta_{m,2}+\delta_{m,-2})^{-1}} \left[\frac{(\ell+2)(\ell+1)\tilde{\Delta}_{Q,\ell-2}}{(2\ell-1)(2\ell+1)} + \frac{6\ell(\ell+1)\tilde{\Delta}_{Q\ell}}{(2\ell+3)(2\ell-1)} + \frac{\ell(\ell-1)\tilde{\Delta}_{Q,\ell+2}}{(2\ell+3)(2\ell+1)} \right], \tag{46}$$

and

$$a_{\ell m}^{\mathrm{B}\,\boldsymbol{k},+} = \frac{-i}{2\sqrt{2}}\sqrt{\frac{2\pi}{(2\ell+1)}}(\delta_{m,2}-\delta_{m,-2})\left[(\ell+2)\tilde{\Delta}_{Q,\ell-1}+(\ell-1)\tilde{\Delta}_{Q,\ell+1}\right]. \tag{47}$$

We have thus shown explicitly that both the E and B components are nonzero for a gravitational wave, confirming the heuristic arguments above.

This particular gravitational wave (in the $\hat{z}$ direction with + polarization) contributes

$$C_\ell^{\mathrm{BB},\,\boldsymbol{k},+} = \frac{1}{2l+1}\sum_m |a_{\ell m}^B|^2 = \frac{\pi}{2}\left[\frac{\ell+2}{2\ell+1}\tilde{\Delta}_{Q,\ell-1} + \frac{\ell-1}{2\ell+1}\tilde{\Delta}_{Q,\ell+1}\right]^2. \tag{48}$$

to the BB power spectrum, and similarly for C_ℓ^{EE}, with the replacement B→E in Equation 48. Since C_ℓ^{BB} is a rotationally invariant quantity, any gravitational wave of this wavenumber k pointing in any direction, with either polarization, will contribute similarly to C_ℓ^{BB}. We thus obtain the BB power spectrum from the stochastic gravitational-wave background by summing all Fourier modes, $\int d^3k/(2\pi)^3$, and over both gravitational-wave polarization states. The final result for C_ℓ^{BB} is thus,

$$C_\ell^{\mathrm{BB}} = \frac{1}{2\pi}\int k^2\, dk \left[\frac{\ell+2}{2\ell+1}\tilde{\Delta}_{Q,\ell-1}(k) + \frac{\ell-1}{2\ell+1}\tilde{\Delta}_{Q,\ell-1}(k)\right]^2, \tag{49}$$

and analogously for C_ℓ^{EE}. Note that the cross-correlation power spectrum vanishes, $C_\ell^{\mathrm{EB}} = \sum_{m=-\ell}^{m=\ell}(a_{\ell m}^{\mathrm{E*}}a_{\ell m}^{\mathrm{B}})/(2\ell+1) = 0$, as it should, because $a_{(\ell m)}^{\mathrm{E}} \propto (\delta_{m,2}+\delta_{m,-2})$, while $a_{(\ell m)}^{\mathrm{B}} \propto (\delta_{m,2}-\delta_{m,-2})$ for a + polarization gravitational wave propagating in the $\hat{z}$ direction, and similarly for C_ℓ^{TB}.

Figure 7 shows results of numerical evaluation of Equation 49 using CAMB (Lewis, Challinor & Lasenby 2000), with the Planck 2015 cosmological parameters (Ade et al. 2015c). The "recombination peak" in the power spectrum [multiplied by $\ell(\ell+1)/2\pi$] at $\ell \sim 100$ arises from gravitational waves that enter the horizon around the time of CMB decoupling at redshift $z \simeq 1100$. The power drops at smaller ℓ because longer-wavelength modes were superhorizon at the time of decoupling and thus have a suppressed effect on subhorizon physics. The power drops at higher ℓ because the amplitudes of shorter-wavelength gravitational waves, which entered the horizon earlier, have begun redshifting away by the time of CMB decoupling. The "reionization bump" at $\ell \lesssim 10$ (Ng & Ng 1996; Zaldarriaga 1997) arises from re-scattering of the CMB by free electrons that were reionized at redshift $z \sim 8$ by ultraviolet radiation from the first stars. The wiggles at higher ℓ arise from the difference in phases of gravitational waves at different wavelengths at the time of CMB decoupling (Pritchard & Kamionkowski 2005; Flauger & Weinberg 2007). The overall amplitude scales with the tensor-to-scalar ratio r.

Line-of-sight and total-angular-momentum formalisms. Numerical solution to the hierarchy of coupled integro-differential equations required to evolve the $\Delta_{Q\ell}(k)$ forward in time from the primordial Universe until today is computationally intensive. They can be
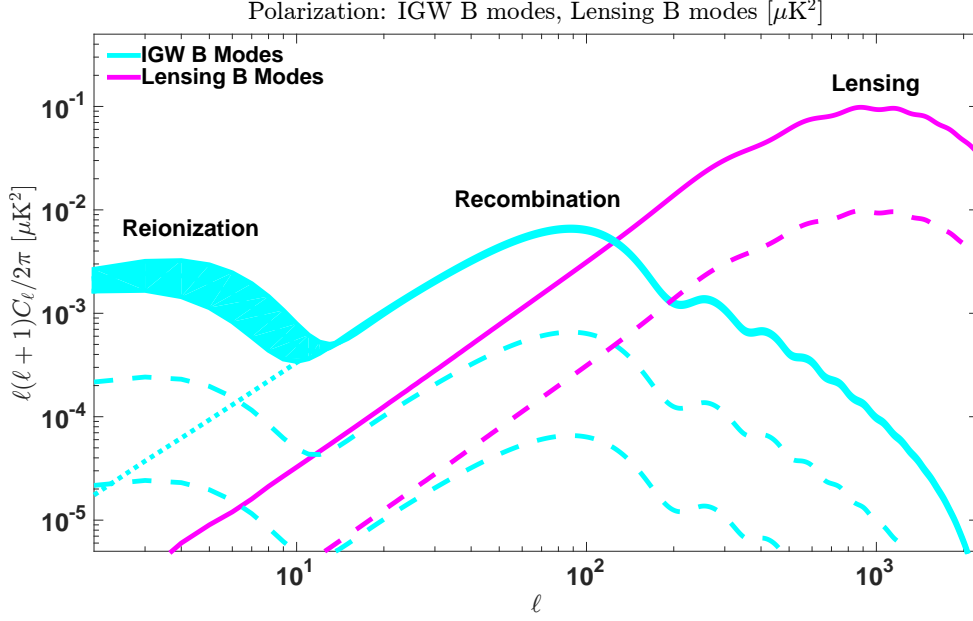
Polarization: IGW B modes, Lensing B modes [μK^2]

Figure 7

Polarization power: Spectra are shown for primordial B modes with $r = \{0.1, 0.01, 0.001\}$ (*cyan*), lensing-induced B modes (*magenta*), as well as scalar E modes (*red*), for comparison. The $\pm 1\sigma$ uncertainty due to the current constraint on τ, the optical depth to reionization, is indicated for the $r = 0.1$ case by the (*cyan*) shading (the dotted line is the result with no reionization). A 90% delensed signal is also shown for comparison (*dashed-magenta*). Plots were generated using CAMB (Lewis, Challinor & Lasenby 2000) with Planck 2015 best-fit parameters (Ade et al. 2015c).

formally integrated (Zaldarriaga & Harari 1995) to provide line-of-sight expressions (Seljak & Zaldarriaga 1996)

$$C_\ell^{\text{EE}} = \int d\ln k \, \Delta_h^2(k) \left\{ \int_0^{\eta_0 - \eta_{\text{ls}}} dx g(\eta_0 - x) \Psi(\eta_0 - x) \left[-j_\ell(x) + j_\ell''(x) + \frac{2j_\ell(x)}{x^2} + \frac{4j_\ell'(x)}{x} \right] \right\}^2$$

$$C_\ell^{\text{BB}} = \int d\ln k \, \Delta_h^2(k) \left\{ \int_0^{\eta_0 - \eta_{\text{ls}}} dx g(\eta_0 - x) \Psi(\eta_0 - x) \left[2j_\ell'(x) + \frac{4j_\ell(x)}{x} \right] \right\}^2, \tag{50}$$

for the EE and BB power spectra, respectively. Here x is a distance along the line of sight and η_0 and η_{ls} the conformal times today and at last scatter, respectively. Also, $g(\eta)d\eta$ is the fraction of CMB photons that last scatter between conformal times η and $\eta + d\eta$. The strange combinations of spherical Bessel functions can be understood as follows. The transverse-traceless part of the three-dimensional spatial metric—i.e., the part that describes gravitational waves—can be decomposed into three-dimensional *total angular momentum* (TAM) waves (Dai, Kamionkowski & Jeong 2012), eigenfunctions of wavenumber k of the Laplacian and of total (orbital plus spin) angular momentum quantum numbers ℓ and m. There are two such sets of TAM waves that can be labeled E and B. The arrangements of spherical-Bessel functions that appear in Equations 50 are then the coefficients [Equation 94

E and B modes from density perturbations. The same lines of reasoning that conclude that both E and B modes are induced by gravitational waves demonstrate that density perturbations do not produce a curl. Consider a single Fourier mode of the density field in the $\hat{z}$ direction. Then the Sachs-Wolfe effect induces an intensity variation proportional to $(\cos^2\theta - 1/3)$. Any electron at the surface of last scatter now sees a quadrupolar intensity variation that is aligned with the $\hat{\theta}$ direction or the direction perpendicular. We thus find that for $\boldsymbol{k}||\hat{z}$, $U(\hat{n}) = 0$, so

$$\mathcal{P}^{ab}(\theta, \phi) = \sum_\ell \sin^2\theta \, \tilde{\Delta}^s_{Q\ell} P_\ell(\cos\theta) \begin{pmatrix} 1 & 0 \\ 0 & -\csc^2\theta \end{pmatrix}, \tag{51}$$

where here $\tilde{\Delta}^a_{Q\ell}$ are the polarization moments for a density perturbation. One finds from this polarization pattern $a^{\mathrm{E}}_{\ell m} \neq 0$, but $a^{\mathrm{B}}_{\ell m} = 0$. This happens because $\mathcal{P}^{ab}\epsilon^c_{\ b} = 0$ which follows since $\mathcal{P}^{ab}$ is diagonal and independent of ϕ. Therefore, a curl component (B mode) in the CMB arises at linear order in perturbation theory only from primordial gravitational waves.

in Dai, Kamionkowski & Jeong (2012)] in the projection from the three-dimensional E and B TAM waves onto the respective two-dimensional polarization tensor spherical harmonics on the surface of the sky.

6. Lensing-induced B modes

Above we showed that density perturbations do not induce a curl in the polarization. However, that derivation assumed only linear perturbations, in which each Fourier mode of the density field is considered independently. B modes may still arise from the density at higher order.

The largest relevant nonlinear effect in the CMB is weak gravitational lensing (or cosmic shear) of the primordial CMB temperature-polarization pattern by density perturbations between us and the CMB surface of last scatter (Zaldarriaga & Seljak 1998; Lewis & Challinor 2006). Lensing displaces the temperature and polarization from a given direction $\boldsymbol{\theta}$ at the surface of last scatter to an adjacent position $\boldsymbol{\theta} + \delta\boldsymbol{\theta}$:

$$\begin{pmatrix} T \\ Q \\ U \end{pmatrix}_{\mathrm{obs.}} (\boldsymbol{\theta}) = \begin{pmatrix} T \\ Q \\ U \end{pmatrix}_{\mathrm{ls}} (\boldsymbol{\theta} + \delta\boldsymbol{\theta}) \simeq \begin{pmatrix} T \\ Q \\ U \end{pmatrix}_{\mathrm{ls}} (\boldsymbol{\theta}) + \delta\boldsymbol{\theta} \cdot \nabla \begin{pmatrix} T \\ Q \\ U \end{pmatrix}_{\mathrm{ls}} (\boldsymbol{\theta}), \tag{52}$$

where $\delta\boldsymbol{\theta} = \nabla\Phi$ is the lensing deflection, and Φ is a projection of the three-dimensional gravitational potential $\Phi(\boldsymbol{x})$ along the line of sight $\hat{n}$.

The generation of B modes by lensing is most easily seen in the flat-sky limit. If there is no B mode at the surface of last scatter, then (cf., Equation 31) $\tilde{Q}(\boldsymbol{\ell}) = 2\tilde{E}(\boldsymbol{\ell})\cos 2\varphi_{\boldsymbol{\ell}}$ and $U(\boldsymbol{\ell}) = -2E(\boldsymbol{\ell})\sin 2\varphi_{\boldsymbol{\ell}}$. Thus,

$$\nabla Q(\boldsymbol{\theta}) = -2i \int \frac{d^2\boldsymbol{\ell}}{(2\pi)^2} \, \tilde{E}(\boldsymbol{\ell}) \, \cos 2\varphi_{\boldsymbol{\ell}} \, \boldsymbol{\ell} \, e^{-i\boldsymbol{\ell}\cdot\boldsymbol{\theta}}, \tag{53}$$

and similarly for $\nabla U(\boldsymbol{\theta})$ with $\cos \to -\sin$. The deflection angle is likewise

$$\tilde{\Phi}(\boldsymbol{\theta}) = -i \int \frac{d^2\boldsymbol{\ell}}{(2\pi)^2} \, \Phi(\boldsymbol{\ell}) \, e^{-i\boldsymbol{\ell}\cdot\boldsymbol{\theta}} \, \boldsymbol{\ell}. \tag{54}$$

Thus, the perturbation to Q and U induced by gravitational waves is

$$\delta Q(\boldsymbol{\theta}) = (\nabla Q) \cdot (\nabla \Phi) = \int \frac{d^2\boldsymbol{\ell}}{(2\pi)^2} e^{i\boldsymbol{\ell}\cdot\boldsymbol{\theta}} (\nabla Q \cdot \nabla \Phi)_{\boldsymbol{\ell}}, \tag{55}$$

where

$$\delta Q(\boldsymbol{\ell}) \equiv [(\nabla Q) \cdot (\nabla \Phi)]_{\boldsymbol{\ell}} = 2 \int \frac{d^2\boldsymbol{\ell}_1}{(2\pi)^2} [\boldsymbol{\ell}_1 \cdot (\boldsymbol{\ell} - \boldsymbol{\ell}_1)] \tilde{E}(\boldsymbol{\ell}_1)\tilde{\Phi}(\boldsymbol{\ell} - \boldsymbol{\ell}_1) \cos 2\varphi_{\boldsymbol{\ell}_1}, \tag{56}$$

$$\delta U(\boldsymbol{\ell}) \equiv [(\nabla U) \cdot (\nabla \Phi)]_{\boldsymbol{\ell}} = -2 \int \frac{d^2\boldsymbol{\ell}_1}{(2\pi)^2} [\boldsymbol{\ell}_1 \cdot (\boldsymbol{\ell} - \boldsymbol{\ell}_1)] \tilde{E}(\boldsymbol{\ell}_1)\tilde{\Phi}(\boldsymbol{\ell} - \boldsymbol{\ell}_1) \sin 2\varphi_{\boldsymbol{\ell}_1}. \tag{57}$$

Although the original map had (by assumption) no curl, the lensed map does; from Equation 30,

$$B(\boldsymbol{\ell}) = \frac{1}{2}[\sin 2\varphi_{\boldsymbol{\ell}}\,\delta Q(\boldsymbol{\ell}) - \cos 2\varphi_{\boldsymbol{\ell}}\,\delta U(\boldsymbol{\ell})] = \int \frac{d^2\boldsymbol{l}_1}{(2\pi)^2}[\boldsymbol{\ell}_1\cdot(\boldsymbol{\ell}-\boldsymbol{\ell}_1)]E(\boldsymbol{\ell}_1)\Phi(\boldsymbol{\ell}-\boldsymbol{\ell}_1)\sin 2\varphi_{\boldsymbol{\ell}_1}. \tag{58}$$

If the power spectrum for the projected potential is $C_\ell^{\Phi\Phi}$, then the B-mode power spectrum from lensing is,

$$C_\ell^{\mathrm{BB}} = \int \frac{d^2\boldsymbol{l}_1}{(2\pi)^2}[\boldsymbol{\ell}_1 \cdot (\boldsymbol{\ell} - \boldsymbol{\ell}_1)]^2 \sin^2 2\varphi_{\boldsymbol{\ell}_1} C_{|\boldsymbol{\ell}-\boldsymbol{\ell}_1|}^{\Phi\Phi} C_{\ell_1}^{\mathrm{EE}}. \tag{59}$$

In **Figure 7** we show numerical results for the lensing B-mode power spectrum (Zaldarriaga & Seljak 1998; Kesden, Cooray & Kamionkowski 2002; Knox & Song 2002). Given the extraordinary current precision of the standard ΛCDM parameters, the predictions for this B-mode spectrum are very precise, especially at the the $\ell \sim 10-100$ range where the gravitational-wave signal peaks. [Neutrino masses (Abazajian et al. 2015b) and/or the effects of nontrivial dark energy may affect lensing-induced B-mode power at larger ℓ (Benson et al. 2014).] These lensing-induced B modes have now been detected in the range $200 \lesssim \ell \lesssim 1500$ by several experiments. Detection through cross-correlation with tracers of the projected potential (see below) was reported by SPTPol (Hanson et al. 2013), POLARBEAR (Ade et al. 2014d), and ACTPol (van Engelen et al. 2015), and then detections in autocorrelation were reported by POLARBEAR (Ade et al. 2014a), BICEP2/Keck (Ade et al. 2014c), and SPTPol (Keisler et al. 2015).

Delensing. As is clear from **Figure 7**, if r is large enough, then the recombination peak in the B-mode power spectrum will stand out (given sufficiently precise experiments) from the lensing power spectrum, and even more so the reionization bump. There are, however, prospects to distinguish the B modes due to lensing from those due to gravitational waves. Measurement of higher-order temperature-polarization correlations induced by lensing can be used to reconstruct the deflection angle, $\delta\boldsymbol{\theta}(\boldsymbol{\theta}) = \nabla\Phi(\boldsymbol{\theta})$, as a function of position on the sky (Zaldarriaga & Seljak 1999; Seljak & Zaldarriaga 1999; Hu & Okamoto 2002; Kesden, Cooray & Kamionkowski 2003), and these may then be used to reduce the lensing-induced curl (Kesden, Cooray & Kamionkowski 2002; Knox & Song 2002; Seljak & Hirata

2004). Heuristically, lensing will stretch the CMB temperature-polarization patterns in some small region of the sky and thus induce a local departure from statistical isotropy, a preferred direction in the temperature-polarization correlations over some small patch of sky. Lensing-reconstruction algorithms then map this local departure from statistical isotropy as a function of position on the sky.

We illustrate this by explaining how lensing reconstruction works with a temperature map and then discuss the generalization to polarization. In the absence of lensing, each Fourier mode $\tilde{T}(\boldsymbol{\ell})$ of the temperature field is statistically independent, $\left\langle \tilde{T}(\boldsymbol{\ell})\tilde{T}(\boldsymbol{\ell}')\right\rangle = 0$, for $\boldsymbol{\ell} \neq \boldsymbol{\ell}'$. However, if there is lensing, an observed Fourier mode $\tilde{T}(\boldsymbol{\ell})$ has contributions from all pairs of temperature and projected-potential Fourier modes $\tilde{T}(\boldsymbol{\ell_1})$ and $\tilde{\Phi}(\boldsymbol{\ell_2})$ that have $\boldsymbol{\ell} = \boldsymbol{\ell_1} + \boldsymbol{\ell_2}$. Thus, with lensing,

$$\left\langle \tilde{T}(\boldsymbol{\ell_1})\tilde{T}(\boldsymbol{\ell_2})\right\rangle = f(\boldsymbol{\ell_1},\boldsymbol{\ell_2})\tilde{\Phi}(\boldsymbol{\ell}) \ \ \text{for} \ \ \boldsymbol{\ell_1} \neq \boldsymbol{\ell_2}, \tag{60}$$

in the presence of some fixed projected potential $\Phi(\boldsymbol{\theta})$ with Fourier components $\tilde{\Phi}(\boldsymbol{\ell})$. Here, $f(\boldsymbol{\ell_1},\boldsymbol{\ell_2}) = C_\ell^{\mathrm{TT}}(\boldsymbol{\ell}\cdot\boldsymbol{\ell_1}) + C_\ell^{\mathrm{TT}}(\boldsymbol{\ell}\cdot\boldsymbol{\ell_2})$. Each $\boldsymbol{\ell_1}$-$\boldsymbol{\ell_2}$ pair of observed temperature modes, with $\boldsymbol{\ell_1} + \boldsymbol{\ell_2} = \boldsymbol{\ell}$, then provides an estimator $\widehat{\Phi}(\boldsymbol{\ell}) = \tilde{T}(\boldsymbol{\ell_1})\tilde{T}(\boldsymbol{\ell_2})/f(\boldsymbol{\ell_1},\boldsymbol{\ell_2})$ for $\tilde{\Phi}(\boldsymbol{\ell})$. The optimal estimator for the Fourier components of projected potential is then obtained by adding, with inverse-variance weighting, all the estimators from all $\boldsymbol{\ell_1}$-$\boldsymbol{\ell_2}$ pairs with $\boldsymbol{\ell_1} + \boldsymbol{\ell_2} = \boldsymbol{\ell}$ (Hu & Okamoto 2002)

$$\widehat{\Phi(\boldsymbol{\ell})} = A(\ell) \int \frac{d^2\boldsymbol{\ell_1}}{(2\pi)^2}\tilde{T}(\boldsymbol{\ell_1})\tilde{T}(\boldsymbol{\ell_2})F(\boldsymbol{\ell_1},\boldsymbol{\ell_2}), \tag{61}$$

$$F(\boldsymbol{\ell_1},\boldsymbol{\ell_2}) \equiv \frac{f(\boldsymbol{\ell_1},\boldsymbol{\ell_2})}{2C_{\ell_1}^{\mathrm{TT,t}}C_{\ell_2}^{\mathrm{TT,t}}}, \qquad A(L) = L^2\left[\int \frac{d^2\boldsymbol{\ell_1}}{(2\pi)^2}f(\boldsymbol{\ell_1},\boldsymbol{\ell_2})F(\boldsymbol{\ell_1},\boldsymbol{\ell_2})\right]^{-1}, \tag{62}$$

where $C_\ell^{\mathrm{TT,t}}$ is the total observed (signal plus noise) power spectrum. Thus, with these estimators, the projected potential can be determined as a function of position across the sky from the measured temperature map. The projected-potential measurement can then be used to "delens" the observed polarization pattern; i.e., to reconstruct the polarization pattern at the surface of last scatter from the (lensed) temperature/polarization pattern that is observed (Kesden, Cooray & Kamionkowski 2002; Knox & Song 2002).

Table 1 **Minimum variance filters for different lensing potential estimators. We define $\varphi_{12} \equiv \varphi_{\boldsymbol{\ell_1}} - \varphi_{\boldsymbol{\ell_2}}$, where $\varphi_{\boldsymbol{\ell_1}}, \varphi_{\boldsymbol{\ell_2}}$ are the angles between $\boldsymbol{\ell_1}, \boldsymbol{\ell_2}$ and the x axis, respectively.**

XX′	$f_{\mathrm{XX'}}(\boldsymbol{\ell_1},\boldsymbol{\ell_2})$	XX′	$f_{\mathrm{XX'}}(\boldsymbol{\ell_1},\boldsymbol{\ell_2})$
TT	$C_{\ell_1}^{\mathrm{TT}}(\boldsymbol{\ell}\cdot\boldsymbol{\ell_1}) + C_{\ell_2}^{\mathrm{TT}}(\boldsymbol{\ell}\cdot\boldsymbol{\ell_2})$	EE	$[C_{\ell_1}^{\mathrm{EE}}(\boldsymbol{\ell}\cdot\boldsymbol{\ell_1}) + C_{\ell_2}^{\mathrm{EE}}(\boldsymbol{\ell}\cdot\boldsymbol{\ell_2})]\cos 2\varphi_{12}$
TE	$C_{\ell_1}^{\mathrm{TE}}(\boldsymbol{\ell}\cdot\boldsymbol{\ell_1})\cos 2\varphi_{12} + C_{\ell_2}^{\mathrm{TE}}(\boldsymbol{\ell}\cdot\boldsymbol{\ell_2})$	EB	$[C_{\ell_1}^{\mathrm{EE}}(\boldsymbol{\ell}\cdot\boldsymbol{\ell_1}) - C_{\ell_2}^{\mathrm{BB}}(\boldsymbol{\ell}\cdot\boldsymbol{\ell_2})]\sin 2\varphi_{12}$
TB	$C_{\ell_1}^{\mathrm{TE}}(\boldsymbol{\ell}\cdot\boldsymbol{\ell_1})\sin 2\varphi_{12}$	BB	$[C_{\ell_1}^{\mathrm{BB}}(\boldsymbol{\ell}\cdot\boldsymbol{\ell_1}) + C_{\ell_2}^{\mathrm{BB}}(\boldsymbol{\ell}\cdot\boldsymbol{\ell_2})]\cos 2\varphi_{12}$

Similar estimators that use polarization, as well as temperature, can be constructed analogously (Hu & Okamoto 2002). There are then in addition to the TT estimator described above, EE, TE, EB, TB, and BB estimators, with coupling coefficients $f(\boldsymbol{\ell_1},\boldsymbol{\ell_2})$ as given in **Table 1**. The precision with which $\tilde{\Phi}(\boldsymbol{\ell})$ can be reconstructed depends on the number of small-scale coherence patches in the temperature-polarization map that can be used as 'sources' with which the shear can be reconstructed. Thus, high angular resolution

and high sensitivity are required. Since the polarization power spectrum peaks at $\ell \sim 1000$, rather than $\ell \sim 200$, there are more small-scale coherence patches in the polarization than in the temperature. Given that there are (under the null hypothesis of no gravitational waves) no B modes in the primordial map, there is no cosmic-variance contribution to the EB lensing estimator, and this turns out to ultimately provide the most power in lensing reconstruction (Hu & Okamoto 2002). Thus, a high-sensitivity and high-resolution polarization map is required to optimize lensing reconstruction.

CMB lensing has recently entered the era of detection. The effects of lensing of the WMAP temperature map were discovered through cross-correlation with the NVSS radio survey (Smith, Zahn & Dore 2007) and several other tracers of the mass distribution (Hirata et al. 2008) and then through autocorrelation in ACT (Das et al. 2011) and SPT (van Engelen et al. 2012). An all-sky map of the projected mass density was more recently constructed from lensing of the Planck maps (Ade et al. 2014f). The effects of lensing on the CMB polarization have now also been detected—these are the B-mode detections discussed above. The possibility to trace the projected potential by using lensing of galaxies (Marian & Bernstein 2007) and 21-cm maps (Sigurdson & Cooray 2005) have also been considered although the latter is somewhat futuristic.

7. Foreground contributions to B modes

The largest IGW B-mode signal allowed by current observational limits is $O(10)\,\mathrm{nK}$, and a sensitivity to a tensor-to-scalar ratio as small as $r \sim 10^{-3}$ implies a B-mode signal four orders of magnitude smaller. Detecting a primordial CMB signal of this amplitude is a daunting task. As polarization is measured in bolometer experiments by taking the difference between the temperature at two orthogonal, co-located axes (once for Q and then at a $45°$ angle for U), uncontrolled variations in temperature along these axes can be mistaken for proper polarization fluctuations. Unfortunately, spread out between us and the last-scattering surface at $z \simeq 1100$, there is a long line of obtruding foregrounds which hinder our ability to accurately measure temperature differences at CMB frequencies. Measurements from the ground are obscured by contributions from man-made electromagnetic interference and atmospheric noise, which contribute at all frequencies. In nearby outer space, zodiacal light (emission from the interplanetary dust cloud) generates pollution on frequencies $\gtrsim 100\,\mathrm{GHz}$. Further out, there are various sources of contamination from localized objects, including inverse-Compton scattering of CMB photons from hot electrons in intracluster gas (the Sunyaev-Zeldovich effect (Sunyaev & Zeldovich 1972, 1980; Birkinshaw 1999)) at $10 - 300\,\mathrm{GHz}$, synchrotron emission from active galactic nuclei at $\lesssim 100\,\mathrm{GHz}$, as well as extragalactic dust emission (the cosmic infrared background, the integrated effect from high-redshift galaxies) at $\gtrsim 100\,\mathrm{GHz}$ (Ade et al. 2014h).

Galactic foregrounds

For large-angular-scale polarization, however, the dominant foregrounds are Galactic in origin, mainly in the form of diffuse synchrotron and thermal dust emissions (free-free emission from accelerated electrons in the ionized gas and *anomalous* dust emission (Kogut et al. 1996; Leitch et al. 1997)—which is most likely due to electric dipole radiation from small spinning dust grains—provide additional subdominant contributions), both of which involve the Galactic magnetic field. Together they render the Galactic plane virtually

BICEP2

In March 2014 the BICEP2 Collaboration reported detection of B-mode power at 150 GHz and $\ell \sim 40-100$ in excess of that expected from lensing (Ade et al. 2014c). The B-mode signal was found to have no correlation with existing dust-polarization templates and to have an amplitude in excess of that expected from dust. The potentially extraordinary implications of this measurement attracted considerable scrutiny, and arguments were made that uncertainties in the various dust templates may have been underestimated (Mortonson & Seljak 2014; Flauger, Hill & Spergel 2014). Data from Planck (Adam et al. 2014) on polarized dust emission at high Galactic latitude then indicated that pre-Planck dust models had underestimated the polarization. A subsequent joint analysis of BICEP2/Keck and Planck data discovered a significant correlation between the BICEP2/Keck 150 GHz polarization map and the Planck 353 GHz map, indicating that the entire BICEP2 B-mode excess could be attributed to dust, leaving an upper limit $r \leq 0.12$ (95% C.L.) to the tensor-to-scalar ratio (Ade et al. 2015a).

unusable for cosmological observations, leaving the sky at high Galactic latitudes as the focus of CMB analysis. In order to extract a CMB signal as clean as possible, a considerable portion of the sky is masked. Multi-frequency measurements are then used in order to separate the components of the radiation in the remaining regions, relying on the fact that their intensities differ in frequency dependence.

Synchrotron. Galactic synchrotron emission is dominant at frequencies below 100 GHz, and both WMAP and Planck have observed its polarization signature at frequencies from 30 to 90 GHz [up until then the only all-sky template was the Haslam map (Haslam et al. 1982), at a much lower frequency of 408 MHz]. These multi-frequency measurements have been used to fit a spectral brightness temperature index of $\beta_s \sim -3$ above 20 GHz (Adam et al. 2015b). As many of the upcoming CMB polarization experiments intend to take data at $\lesssim 90$ GHz, improved understanding of this foreground is essential.

Dust. Above 100 GHz, thermal emission from asymmetric dust grains in the interstellar medium, which align themselves with the Galactic magnetic field, induces a strong polarization signal, which depends on the composition, shape and size of the grains (Draine & Fraisse 2009; Martin 1971; Ali-Haimoud 2013; Andersson et al. 2015). Early templates for Galactic dust were based on smoothed maps of starlight polarization (Page et al. 2007). While starlight polarization has been demonstrated to be a good tracer of dust polarization (Ade et al. 2015e), this approach is limited by the sparsity of the data and the fact that the stars reside at different distances. Other templates have relied heavily on models for the Galactic magnetic field, and over the years several such models have been developed [e.g., (O'Dea et al. 2012; Delabrouille et al. 2013)]. In the absence of solid observational data, however, theoretical templates inevitably involve considerable guesswork, and theoretical templates of Galactic dust-emission foregrounds before the advent of high-frequency data from the Planck satellite turned out to underestimate the amplitude of dust polarization at high Galactic latitudes.

The Planck High Frequency Instrument (HFI) has recently provided full-sky tempera-

ture and polarization maps at frequencies ranging from 100 to 857 GHz (corresponding to 3 mm to 350 μm wavelengths). Focusing on 353 GHz data at high Galactic latitudes, the E and B angular power spectra of dust polarization were constrained in the multipole range $40 < \ell < 600$ (Adam et al. 2014). The frequency dependence was found to be consistent with a modified blackbody emission with power-law emissivity $\epsilon_\nu \propto \nu^{\beta_d}$ and temperature T_d with best-fit values $\beta_d = 1.59$ and $T_d = 19.6$ K. It was also shown that both C_ℓ^{EE} and C_ℓ^{BB} spectra are well described by power laws with exponents $\alpha_{EE,BB} = -2.42 \pm 0.02$, almost independent of the region of sky. The amplitudes, however, were shown to vary considerably across the sky. While no region of sky was found to be clean enough to enable IGW detection without foreground subtraction, Planck did identify in each Galactic hemisphere several patches of sky at high Galactic latitudes with considerably lower foreground amplitudes, possibly useful targets for future IGW B-mode searches.

Dust-polarization puzzles. While dust and lensed E modes provide a satisfactory fit to all current measurements, several results remain unexplained. For example, both WMAP (Page et al. 2007) and Planck (Adam et al. 2014) have found a systematic difference in amplitude between dust E and B modes, roughly $C_\ell^{\mathrm{BB}} = 0.5 C_\ell^{\mathrm{EE}}$, almost independent of Galactic latitude. This disagrees with the expectation $C_\ell^{\mathrm{BB}} \simeq C_\ell^{\mathrm{EE}}$ if the polarization orientation is coherent over large patches with small-scale modulations in amplitude (Zaldarriaga 2001; Kamionkowski & Kovetz 2014). It has been postulated that this could be explained by magnetohydrodynamic turbulence in the interstellar medium (Hirata 2014).

In addition, the frequency dependence of the dust polarization fraction as observed by Planck [see **Figure 13** in Ade et al. (2014i)] has an opposite trend compared to the long-standing predictions from models of silicate or carbonaceous dust grains (see **Figure 8** of Draine & Fraisse (2009)). Models involving magnetic nanoparticles (namely ferromagnetic or ferrimagnetic iron grains) (Draine & Hensley 2013) may explain the observed increase of polarization dust fraction with frequency.

It is also reasonable to wonder whether foreground polarizations measured at different frequencies trace the same depths in the ISM, and thus have the same polarization pattern on the sky (a tacit assumption in such analyses). The correlation between the BICEP2 150 GHz maps and the Planck 353 GHz maps (Ade et al. 2015a) suggest that they do to some extent, but the detailed validity of this assumption warrants further study.

8. The Search for B modes

We now consider the prospects to achieve an experimental sensitivity to a tensor-to-scalar ratio $r \sim 10^{-3}$ and discuss experimental issues and strategies.

8.1. Detectability basics

In principle, an experiment provides the polarization Stokes parameters Q and U at each point on the sky from which the $2\ell + 1$ spherical-harmonic coefficients $a_{\ell m}^{\mathrm{BB}}$ are then obtained from Equation 41. The theory predicts that each of these $a_{\ell m}$ is drawn from a Gaussian distribution with variance $C_\ell^{\mathrm{BB}} = \langle |a_{\ell m}^{\mathrm{BB}}|^2 \rangle$. We thus construct an estimator $\widehat{C_\ell^{\mathrm{BB}}} = \sum_{m=-\ell}^{\ell} |a_{\ell m}|^2/(2\ell+1)$, and this estimator has a root-variance $(\Delta C_\ell^{\mathrm{BB}}) = [2/(2\ell+1)]^{1/2} C_\ell^{\mathrm{BB}}$ (since the root-variance with which we can measure the variance σ^2 of a Gaussian distribution from N measurements is $(2/N)^{1/2}\sigma^2$).

In practice, things are complicated by detector noise in the measurement, imperfectly subtracted foreground contributions to the CMB polarization, and the fact that measurements may be available only over a fraction f_{sky} of the sky. If we are interested to detect IGW-induced B modes, there is also contamination from lensing-induced B modes. The estimator for C_ℓ^{igw} (for notational economy, we drop the BB superscript in the remainder of this section) is then obtained by subtracting from the measured C_ℓ the expected contributions C_ℓ^{lens}, C_ℓ^{fg}, and C_ℓ^{n} from lensing, imperfectly subtracted foregrounds, and detector noise, respectively. The root-variance with which we can measure C_ℓ^{igw} then becomes $(\Delta C_\ell) = [2/(2\ell+1)f_{\text{sky}}]^{1/2} \left(C_\ell^{\text{igw}} + C_\ell^{\text{lens}} + C_\ell^{\text{fg}} + C_\ell^{n} \right)$. The increase by $f_{\text{sky}}^{-1/2}$ in the root variance arises from the decrease in sky coverage.

To evaluate the detectability of IGW B modes, we parametrize the IGW-induced B-mode power spectrum $C_\ell^{\text{igw}} = 10\, r\, C_\ell^{\text{igw}}(r = 0.1)$ in terms of the power spectrum $C_\ell^{\text{igw}}(r = 0.1)$ for a tensor-to-scalar ratio $r = 0.1$, and an amplitude r. Each measured multipole moment C_ℓ^{obs} then provides an estimator $\widehat{r}^\ell = 0.1\,(C_\ell^{\text{obs}} - C_\ell^{\text{lens}} - C_\ell^{\text{fg}} - C_\ell^{\text{n}})/C_\ell^{\text{IGW}}(r = 0.1)$ to the amplitude r. The error to this estimator, under the null hypothesis $r = 0$, is $(\sigma_r^\ell)^2 = 0.01\,[2/(2\ell+1)](C_\ell^{\text{lens}} + C_\ell^{\text{n}} + C_\ell^{\text{fg}})^2$. These estimators can then be added with inverse-variance weighting to obtain the minimum-variance estimator for r. This estimator will have a root-variance,

$$\sigma_r \simeq \frac{0.1}{f_{\text{sky}}} \left(\sum_{\ell=\ell_{\text{min}}}^{\ell_{\text{max}}} \frac{(2\ell+1)}{2} \left[\frac{C_\ell^{\text{IGW}}(r = 0.1)}{C_\ell^{\text{fg}} + C_\ell^{\text{n}} + C_\ell^{\text{lens}}} \right]^2 \right)^{-1/2}, \tag{63}$$

for an experiment that covers a fraction f_{sky} of the sky and measures multipole moments from a minimum ℓ_{min} to a maximum ℓ_{max}.

8.2. The effects of different contaminants

8.2.1. Lensing-induced B modes.
Before including the effects of foregrounds and detector noise, let us first consider the signal-to-noise available in the hypothetical situation of a no-noise and foreground-free measurement; i.e., $C_\ell^{\text{n}} = C_\ell^{\text{fg}} = 0$. In this case there would be a cosmic-variance limit to the measurement of r from lensing-induced B modes, and **Figure 8** plots the summand in Equation 63 as a function of ℓ. As shown there, the vast majority ($\gtrsim$ 99%) of the signal-to-noise on the sky is in the reionization bump, at $\ell \lesssim 10$ (Kamionkowski & Kosowsky 1998); only $\sim 1\%$ is at $\ell \gtrsim 10$. If we were to restrict measurements to $\ell \gtrsim 10$, the vast majority of the signal-to-noise is at $\ell \lesssim 150$ (the recombination bump in C_ℓ^{IGW}).

Evaluating the sum in Equation 63, we can calculate σ_r, the smallest detectable (at 1σ) tensor-to-scalar ratio r, for experiments with access to different multipole ranges. For $2 \leq \ell \leq 10$, we get $\sigma_r \simeq 4 \times 10^{-5}\,(\tau/0.078)^{-2}$, while for $10 \lesssim \ell \lesssim 150$ we get $\sigma_r \simeq 3 \times 10^{-4}\,f_{\text{sky}}^{-1/2}$ (Lewis, Challinor & Turok 2002; Knox & Song 2002; Kesden, Cooray & Kamionkowski 2002). Here we have included the $\propto \tau^{-2}$ scaling with the reionization optical depth (Ng & Ng 1996; Zaldarriaga 1997) for the low-ℓ measurement and the $f_{\text{sky}}^{-1/2}$ scaling for the high ℓ. Although (with no foregrounds) the vast majority of the signal-to-noise is at $\ell \lesssim 10$, an experiment that maps only $\sim 1\%$ of the sky (and thus uses only $\ell \gtrsim 10$) could still have a $\gtrsim 3\sigma$ sensitivity to a tensor-to-scalar ratio as small as $r \sim 0.01$, even with no delensing. As we will see below, delensing by a factor of 10 is conceivable with forthcoming experiments in which case $r \sim 0.001$ could be detected at $\gtrsim 3\sigma$, even with $f_{\text{sky}} \sim 1\%$.
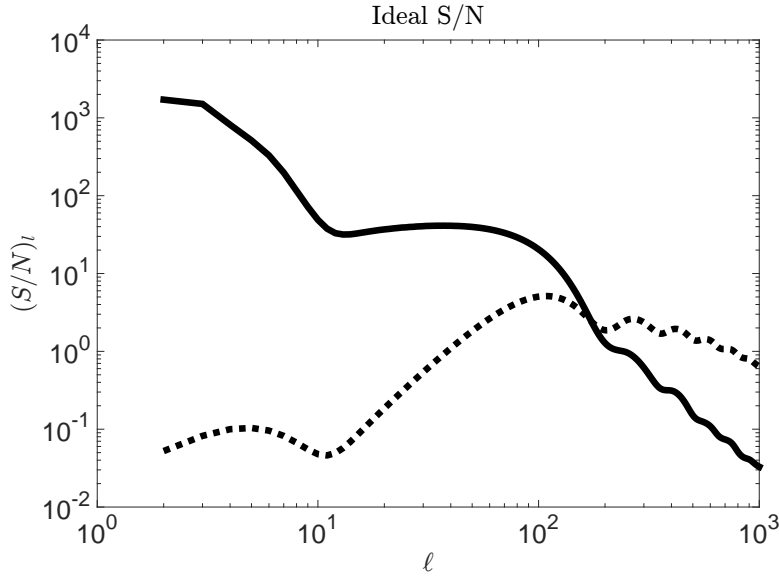
Figure 8

The summand from Equation 63, for the detectability of IGW B modes, with (i) $C_\ell^{\mathrm{fg}} = 0$—i.e., in the absence of foregrounds but with detector noise and lensing-induced B modes included—and (ii) $C_\ell^{\mathrm{n}} = C_\ell^{\mathrm{lens}} = 0$—i.e., in the absence of lensing-induced B modes and detector noise. This figure shows the contributions of various multipole moments to the signal-to-noise assuming the hypothetical situations of (i) no foregrounds, or (ii) no detector noise nor lensing.

8.2.2. Detector noise. We now include the effects of detector noise, still ignoring foregrounds. The power spectrum induced by detector noise is $C_\ell^{\mathrm{n}} = 4\pi f_{\mathrm{sky}} \mathrm{NET}_{\mathrm{array}}^2 / t_{\mathrm{obs}}$ (for multipole moments $\ell \lesssim \theta_{\mathrm{fwhm}}^{-1}$ accessible with a beam width θ_{fwhm}), where the noise equivalent temperature (NET) of the array is defined as $\mathrm{NET}_{\mathrm{array}} = s/\sqrt{N_{\mathrm{det}}}$ in terms of the noise-equivalent temperature s of each detector and the number N_{det} of detectors in the array. Here t_{obs} is the integration time on this fraction f_{sky} of the sky. We now note that the lensing-induced power spectrum is also well approximated by a constant $C_\ell^{\mathrm{lens}} \simeq 1.8 \times 10^{-6} \ \mu\mathrm{K}^2$ over the range $\ell \lesssim 150$ of interest here. (Powers are also sometimes quoted as a sensitivity $(C_\ell)^{1/2}$, wherein the lensing power is 4.6 μK-arcmin.) The distribution of signal-to-noise with ℓ is, with detector noise, thus again exactly as shown in **Figure 8**.

The f_{sky} scaling of C_ℓ^{n} for an experiment that limits its observations to a fraction f_{sky} of the sky implies that a lower C_ℓ^{n} can be achieved by integrating deeply on a smaller patch of sky. This has important implications (Jaffe, Kamionkowski & Wang 2000; Keating, et al. 2003), as discussed below, for the choice of the fraction of the sky surveyed, especially for many of the suborbital experiments that cannot access $\ell \lesssim 10$.

8.2.3. Foregrounds. As discussed above, the principal foregrounds—synchrotron and dust emission from the Milky Way—can be disentangled using measurements of the polarization at multiple frequencies. There will, however, always be some residual foreground contribution to any realistic CMB polarization map. Here we use the scalings, $C_\ell^{\mathrm{fg}} \propto \ell^{-2.42}$

determined empirically for WMAP and Planck for $\ell \gtrsim 40$, and we assume that this scaling extends down to $\ell \lesssim 10$ (although the validity of this assumption is unknown). We set the foreground amplitude to the best-fit values measured by Planck at $353\,\mathrm{GHz}$ on scales $40 < \ell < 370$ over the BICEP2 field, extrapolated down to $150\,\mathrm{GHz}$ (see (Kovetz & Kamionkowski 2015) for details on the extrapolation). The contributions to the signal-to-noise with which a nonzero value of r can be distinguished from the null hypothesis $r = 0$, assuming no detector noise nor lensing, are then shown in **Figure 8**. They are distributed more evenly in ℓ than the summands assuming no foregrounds, with a significant peak at $\ell \sim 100$.

8.3. Experimental strategies

Above we saw roughly speaking the effects of different contaminants on the IGW detectability. These considerations are ingredients in the development of experimental strategies to detect IGWs. These ingredients must then be amalgamated with a number of logistical/experimental/hardware issues—e.g., detector technologies and sensitivities; atmospheric frequency windows; the availability of telescopes; funding constraints; etc.—in the development of experiments. Here we discuss some of the issues, illustrate some of the tradeoffs, and summarize some of the strategies currently being considered.

We begin by plotting in Figure 9 in a unified but somewhat unconventional way the contributions of the various ingredients to the signal-to-noise. The IGW B-mode signal is plotted as $\sqrt{(2\ell+1)/2}\,C_\ell^{\mathrm{igw}}$ for three fiducial values for the tensor-to-scalar ratio, $r = \{0.1, 0.01, 0.001\}$. The prefactor $\sqrt{(2\ell+1)/2}$ is chosen since $(C_\ell^{\mathrm{igw}})^2$ is multiplied by the square of this factor in the expression, Equation 63, for the signal to noise. The foreground, noise, and lensing B modes signals are then plotted with *no* scaling ℓ prefactor. In this way, the contributions of foregrounds, noise, and lensing to the signal-to-noise with which a nonzero value of r can be distinguished from the null hypothesis $r = 0$ are represented viscerally.

For the foregrounds, the amplitude of the plotted signal is taken to match the best-fit value measured by Planck over the BICEP2 field, as explained above. The foregrounds in other regions of sky may be smaller or larger. The foregrounds can be reduced, though, relative to what we have shown, with multi-frequency measurements, as we discuss below. For illustration, we also show noise power spectra for the CLASS (predicted) and BICEP2 instruments, as well as the planned CMB-S4 sensitivity (see below), plotted as C_ℓ^n (i. e., without the $\sqrt{(2\ell+1)/2}$ scaling) on the scales accessible given their beam size. The parameters sets $\{t_{\mathrm{obs}}, \mathrm{NET}_{\mathrm{array}}, f_{\mathrm{sky}}\}$ used for the noise estimates for BICEP2, CLASS and CMB-S4 (assuming 10^5 detectors) are $\{590\,\mathrm{days}, 18.75\,\mu\mathrm{K}\sqrt{\mathrm{sec}}, 0.01\}$, $\{3\,\mathrm{yrs}, 7\,\mu\mathrm{K}\sqrt{\mathrm{sec}}, 0.7\}$ and $\{2\,\mathrm{yrs}, 1.5\,\mu\mathrm{K}\sqrt{\mathrm{sec}}, 0.75\}$, respectively.

We next calculate σ_r as a function of various experimental parameters. We evaluate Equation 63 under the null hypothesis ($C_\ell^{\mathrm{igw}} = 0$), replacing $C_\ell^{\mathrm{lens}} \to (1 - \alpha_L)C_\ell^{\mathrm{lens}}$ and $C_\ell^{\mathrm{fg}} \to \beta_{\mathrm{fg}}C_\ell^{\mathrm{fg}}$, where $1 - \alpha_L$ parametrizes the residual lensing contribution after delensing, and β_{fg} parametrizes the residual foregrounds after multifrequency component separation. While imperfect subtraction can lead to a residual bias in r (Katayama & Komatsu 2011; Remazeilles et al. 2015), note that we consider here only the contribution to the variance. The detector noise is directly proportional to $\mathrm{NET}_{\mathrm{array}}^2$, while the dependence of C_ℓ^n on f_{sky} introduces a tradeoff between the detector noise and the other contributions. The effects of these parameters on σ_r are shown in **Figure 10**.

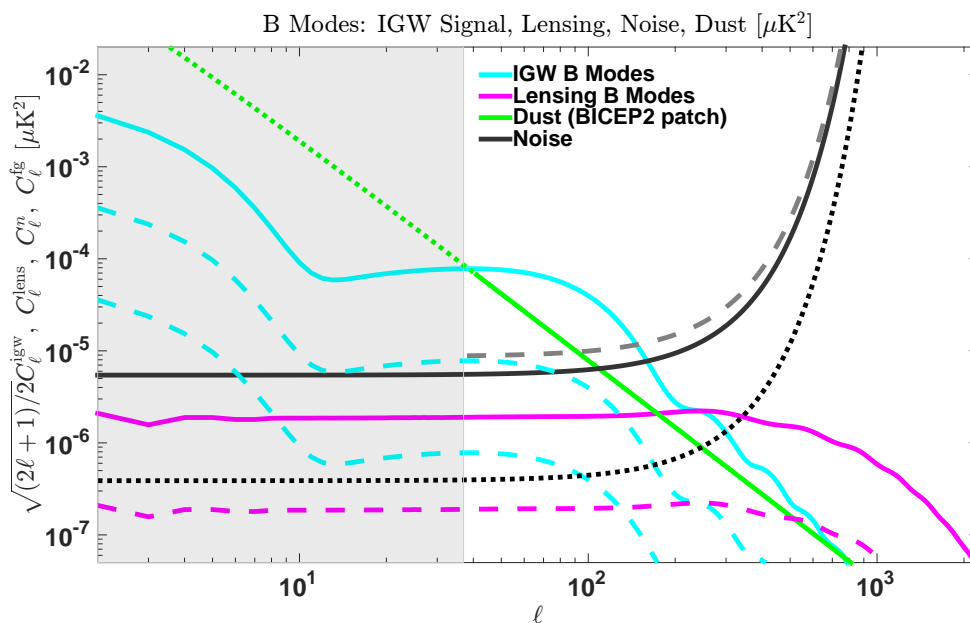B Modes: IGW Signal, Lensing, Noise, Dust $[\mu K^2]$

Figure 9

Balance of Power: Spectra with $\sqrt{(2\ell+1)/2}$ scaling are shown for primordial B modes with $r = \{0.1, 0.01, 0.001\}$ (*cyan*), lensing of primordial E modes (*magenta*) and a fiducial dust foreground (*green*). The amplitude and shape of this fiducial foreground were set to the best-fit values measured by Planck at 353 GHz on scales $40 < \ell < 370$ over the BICEP2 field, extrapolated down to 150 GHz. Whether this extends to larger scales is unknown. Noise spectra are plotted (without the $\sqrt{(2\ell+1)/2}$ scaling) for the CLASS (*solid black*), CMB-S4 (*dotted-black*) and BICEP2 (*dashed-gray*) experiments. Scales inaccessible to BICEP2 due to its limited sky coverage are shaded (*light gray*).

8.3.1. Sky coverage.

Small-sky strategy (no lensing). If access to the reionization peak at $\ell \lesssim 10$. is unavailable, and in the ideal case of no lensing, the ideal B-mode observation is achieved by prolonged integration on a ~ 25-square-degree patch of sky (Jaffe, Kamionkowski & Wang 2000). This is demonstrated in Figure 10, where there is a sweet spot in the two cases where the detector noise is dominant compared to the other contributions. The sensitivity weakens on larger patches because of the increase in C_ℓ^n with $f_{\rm sky}$. The sensitivity then weakens on smaller patches because the decrease in the signal for measurements restricted to $\ell \gtrsim 100$ that then miss much of the recombination peak.

Lensing and the small-sky strategy. If an experiment has noise $C_\ell^n \gtrsim (1-\alpha_L)C_\ell^{\rm lens}$, then the measurement will be detector-noise dominated, and it will be cosmic-variance (lensing) limited otherwise. In the former case, the sensitivity of the measurement to r may be improved by decreasing the sky coverage of the survey; the $f_{\rm sky}$ reduction in C_ℓ^n overtakes the $f_{\rm sky}^{-1/2}$ statistical increase in the prefactor of Equation 63 (Jaffe, Kamionkowski & Wang 2000). Still, as $f_{\rm sky}$ is reduced, $\ell_{\rm min}$ is increased, and if $f_{\rm sky}$ is reduced too much, then
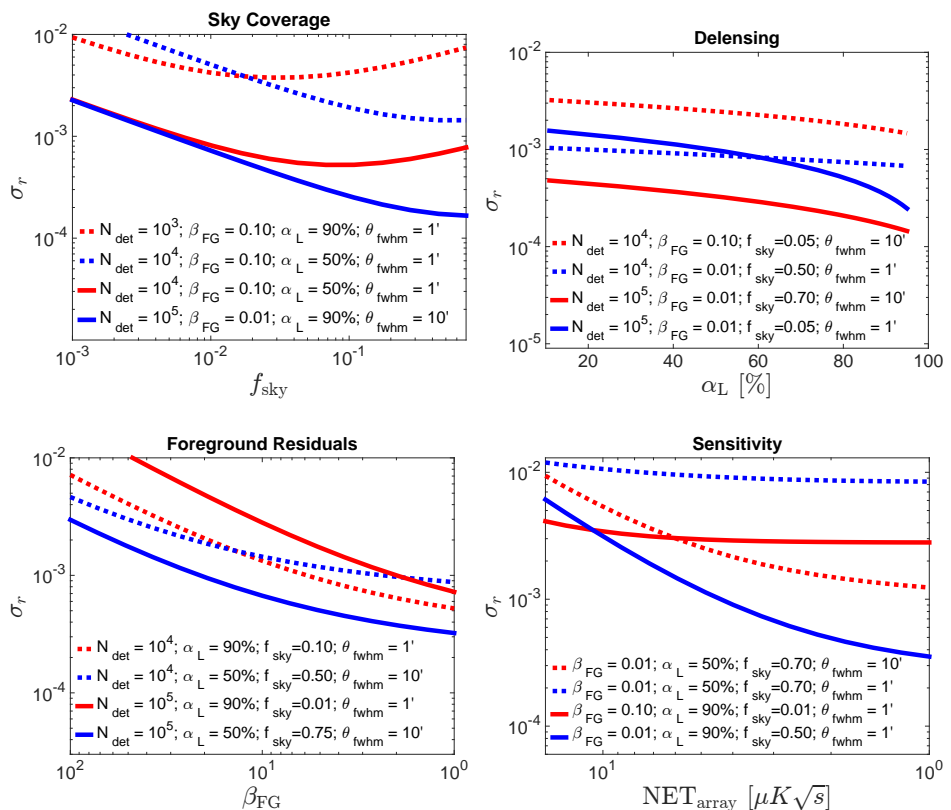
Figure 10

Smallest detectable tensor-to-scalar ratio r: we show the dependence on the sky coverage f_{sky}, delensing efficiency (where $1 - \alpha_L$ quantifies the lensing residual), foregrounds (where β_{fg} denotes the fractional amount of foreground residuals from the fiducial value we have assumed here, see **Figure 9**) and detector sensitivity (through $\text{NET}_{\text{array}}$). We show how the smallest detectable tensor-to-scalar r (at 1σ) depends on each parameter, while all other parameters are held fixed according to different scenarios, which are chosen to cover the range of interesting cases. We adopt the instrumental sensitivity considered in Wu et al. (2014), i. e. a NET per detector of $s = 350 \, \mu\text{K}\sqrt{\text{sec}}$, assume a total of 2 years of observation, and use the fiducial amplitude of dust polarization from **Figure 9**.

the reduction in the signal-to-noise (the area under the curve in **Figure 8**) outweighs the reduction in C_ℓ^{n}.

Once the detector-noise contribution to the power spectrum is reduced to $C_\ell^{\text{n}} \lesssim 2 \times 10^{-6} \, \mu\text{K}^2 \simeq C_\ell^{\text{lens}}$, this small-sky strategy must be revisited (Kesden, Cooray & Kamionkowski 2002; Verde, Peiris & Jimenez 2006). In Figure 10, it is evident, for example, that when the detector noise is high (i. e., comparable to or higher than the lensing contribution), there is nothing to gain by delensing. However, as we begin to access smaller tensor-to-scalar ratios, delensing becomes increasingly important. Further improvements in sensitivity to r must then come from increased sky coverage, to deal with the lensing-induced cosmic variance, or from delensing (discussed more below), to directly reduce the lensing contribution. In practice, the small-sky strategy has already been pursued on larger,

$\sim$ 400-square-degree, patches to deal with systematic effects and foregrounds, for redundancy, and to avoid the lensing contribution, which rises (relative to the IGW contribution) rapidly with ℓ. Given the rapid improvements in $\mathrm{NET}_{\mathrm{array}}$, the lensing issue will become increasingly important.

The large-sky strategy. If an experiment can map the polarization over most of the sky, then it can access the huge amount of information in the reionization peak, $\ell \lesssim 10$. Lensing will not be an issue for the foreseeable future for such an experiment, but such a strategy will require effective isolation of foregrounds. See, e.g., Watts et al. (2015) for a discussion of the large-sky strategy.

Regardless of the strategy (small-sky or large-sky), any experiment will never be able to use data from the entire sky. Techniques have therefore been developed to apply the E/B decomposition on a cut sky (Lewis, Challinor & Turok 2002; Hu, Hedman & Zaldarriaga 2003; Smith 2005; Pearson, Sherwin & Lewis 2014).

8.3.2. Beam size. Since C_ℓ^{igw} decays exponentially at $\ell \gtrsim 100$, high angular resolution is not strictly needed in order to detect IGW B modes. If the CMB map is to be used for delensing, however, it will require very high angular resolution, as discussed below.

8.3.3. Detector noise. The dependence on the sensitivity of the instrument is more straightforward. Figure 10 shows how improved sensitivity can lead to better sensitivity to r given the choice of other parameters. As discussed above, the sensitivity of the small-sky strategy is limited only by detector noise as long as $C_\ell^{\mathrm{n}} \gtrsim C_\ell^{\mathrm{lens}}$, and further improvements to the sensitivity, in the absence of delensing, then drive the survey to larger sky fractions. Given, however, that $C_\ell^{\mathrm{n}} \propto f_{\mathrm{sky}}^{-1/2}$, the detector noise must continue to improve in order for the detector-noise power C_ℓ^{n} to continue to remain smaller than C_ℓ^{lens} as f_{sky} is increased.

8.3.4. Frequency coverage. The dependence on the frequency coverage is harder to quantify and depends on the desired sensitivity to r; on the relative contributions of dust and synchrotron emission (which may depend on the region(s) of sky covered); atmospheric windows (for terrestrial observations); the technologies and sensitivities available at the different frequencies; and the availability of reliable external templates for the foreground polarization. It is clear, though, that measurements in more frequencies over the same patch will enable better foreground removal (as discussed above, the main foreground contributions, due to synchrotron and dust emission, quickly dominate as one pulls away in frequency to either side of the CMB observability peak at $\sim 100\,\mathrm{GHz}$). In Figure 10, we examine the effect of lower foreground residuals under several scenarios for the remaining experimental parameters.

8.3.5. Delensing. We have swept a huge amount of dirt under the rug through the introduction of the delensing parameter α_L, as delensing will be an ambitious, sophisticated, and challenging endeavor. One possibility is that delensing may be done with external data sets that can be used to map the lensing potential. For example, measurements of the cosmic infrared background (CIB) currently provide as good a lensing template as anything else (Sherwin & Schmittfull 2015), and forthcoming galaxy surveys, like LSST, may reduce the lensing B modes by a factor ~ 2 (Marian & Bernstein 2007). However, the most likely source for delensing at the level required to access $r \sim 0.001$ will be small-angular-scale

fluctuations in the CMB.

Although it may ultimately be done by an experiment that also measures the $\ell \lesssim 150$ IGW B modes, a delensing measurement requires angular resolution far better (up to $\ell \sim 2000$) than that required for IGW B modes. A measurement with resolution required to reach multipole moment ℓ at wavelength λ requires a dish of size $D \sim \lambda \ell \sim 4\,\mathrm{meter}\,(\ell/2000)(\nu/150\,\mathrm{GHz})^{-1}$, and so the telescope-diameter requirements for delensing are roughly ten times those for the IGW B modes. Delensing is also optimized with high-angular-resolution maps of the polarization, as well as temperature. The precise level of delensing depends on a variety of experimental parameters, as discussed, for example, in Smith et al. (2012) and Simard, Hanson & Holder (2015). However, to illustrate, we note that the lensing-induced B-mode power may be reduced by a factor ~ 5 with a polarization map with a beam size ~ 5 arcmin and noise level $1\,\mu\mathrm{K}$. The SPT-3G project expects to be able to delens by a factor ~ 4 by 2019 (Benson et al. 2014).

8.4. Current/forthcoming experiments

We now provide a brief listing of some of the experiments underway, in development, or being discussed. There are several that focus a single telescope on a chosen patch of sky to target the recombination peak and perhaps, if the detector-noise level warrants, delens with higher-resolution data from the same experiment or from external datasets. Current and future experiments belonging to this class include: ABS (Staggs et al. 2015), ACTPol (Naess et al. 2014) and its successor AdvACT, the BICEP/KECK series (Ade et al. 2014b, 2015b), POLARBEAR and the future Simons Array (Arnold et al. 2014), and SPTPol (Hanson et al. 2013) and its successor SPT-3G (Benson et al. 2014). A similar strategy is employed by the QUBIC interferometer (Battistelli et al. 2012). There are then a smaller number of sub-orbital projects that employ a wide–sky-coverage telescope, or aggregate several ground-based telescopes, and pursue the reionization scales $\ell \lesssim 10$. Typically, ground-based telescopes can reach higher resolution compared to satellites, which may enable a more efficient delensing process. CLASS (Essinger-Hileman et al. 2014), with $\gtrsim 70\%$ sky-coverage, is one experiment of this type, while under the CMB-S4 plan, several ground-based telescopes such as those above are planned to collaborate in generating a combined, nearly full-sky, map (Wu et al. 2014; Abazajian et al. 2015a). Balloon-borne CMB experiments have less adaptivity and observing time than ground-based telescopes, but they experience less atmospheric interference and can access higher frequencies which may enable more efficient component separation. EBEX (Reichborn-Kjennerud et al. 2010), LSPE (Aiola et al. 2012), PIPER (Lazear et al. 2014), and SPIDER (Crill et al. 2008), are balloon experiments, the latter two of which target larger areas of the sky than most of the small-sky ground-based missions. There are then discussions of a satellite to take full-sky polarization data and fully capture the reionization peak. Proposals for future missions include COrE (Armitage-Caplan et al. 2011), CMBPOL (Baumann et al. 2009), EPIC (Bock et al. 2009), PIXIE (Kogut et al. 2011), PRISM (André et al. 2014) and LiteBIRD (Matsumura et al. 2013). A satellite experiment could also map the full sky with sufficiently high resolution to delens the entire sky and thus use the IGW information also in the recombination peak. Such a mission would, however, require a far larger mirror and thus be more costly. It would, however, also enable a broad range of interesting high-ℓ science apart from IGW B modes. More details about possible future experimental endeavors can be found in Abazajian et al. (2015a) and Baumann et al. (2009). See also Creminelli et al. (2015).

8.5. Mitigating dust

As discussed above, Planck has identified a handful of relatively clean ~ 400-square-degree patches of sky accessible to observatories in the southern hemisphere. Given Planck's noise limitations, however, it is still unclear whether any of these patches is far cleaner, and thus a better B-mode target, than the others, and if so which one. One possibility is a brief initial high-frequency integration (Kovetz & Kamionkowski 2015), either from the ground (at 220 GHz) or 353 GHz (from a balloon) to identify the cleanest such patch before beginning a deep B-mode integration at lower (CMB) frequencies. Such a strategy can conceivably improve the ultimate sensitivity to r by a factor of 2–3 over a blind selection of one of the cleanest patches. It would also provide high-signal-to-noise dust-polarization templates on all six of these regions. There are also adaptive-survey strategies (Kovetz & Kamionkowski 2016) that can be employed to seek low-dust-amplitude regions while simultaneously performing a B-mode integration.
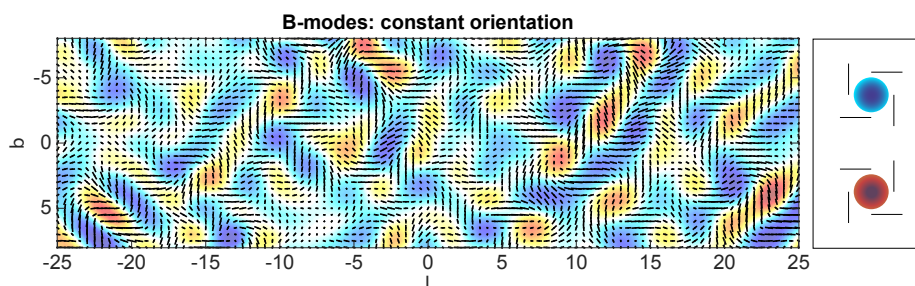

Figure 11

A B-mode map calculated from a randomly generated, statistically isotropic Q map and a $U = 0$ map, to simulate a constant polarization orientation. Here, there is a local hexadecapolar departure from statistical isotropy, dominated by Fourier modes oriented at $45°$ with respect to the polarization orientation. More generally, the local departures from statistical isotropy due to a slowly-varying orientation angle can be captured with appropriate statistical estimators (Kamionkowski & Kovetz 2014). (Compare with bottom of **Figure 6**.)

There are additional cross-checks that can be employed in the event that a nominal IGW B-mode signal is identified even after multifrequency component separation. While the gravitational-wave signal is expected to be Gaussian, the B modes from dust contamination are should be highly non-Gaussian (as are the lensing-induced B modes; in fact it is their characteristic non-Gaussianity that allows them to be delensed). If, for example, the orientation of the dust-induced polarization is relatively coherent on large patches of the sky, which may be expected given the large-scale coherence of Galactic magnetic fields, then the resulting B modes will have a locally hexadecapolar departures from statistical isotropy, composed primarily of Fourier modes aligned primarily in directions $45°$ with respect to the polarization orientation (Zaldarriaga 2001; Kamionkowski & Kovetz 2014). Statistical estimators to seek this type of departure from statistical isotropy are then easily constructed (Kamionkowski & Kovetz 2014) in analogy with lensing-reconstruction estimators. To illustrate, we show in **Figure 11** the hexadecapolar symmetry which results from having a constant orientation angle over the observed sky patch.

Chiral gravitational waves.

As discussed above, TB and EB cross-correlations may arise if the physics that gives rise to CMB temperature/polarization fluctuations is parity breaking. Chiral gravitational waves—a gravitational-wave background with an asymmetry between the density of right- and left-circularly polarized gravitational waves—provide a mechanism to induce such parity-violating correlations (Lue, Wang & Kamionkowski 1999; Contaldi, Magueijo & Smolin 2008). Chiral GWs arise if there is a Chern-Simons modification to gravity (Jackiw & Pi 2003; Alexander & Yunes 2009) during inflation (Lue, Wang & Kamionkowski 1999), a parity-breaking gravitational action during inflation (Contaldi, Magueijo & Smolin 2008), or if inflation involved Horava-Lifshitz gravity (Takahashi & Soda 2009). Chiral gravitational waves also arise in models of inflation with a background gauge field (Maleknejad, Sheikh-Jabbari & Soda 2013; Adshead, Martinec & Wyman 2013), and an analogous mechanism could also work in the late Universe (Bielefeld & Caldwell 2015). The chirality of the GW background may also be connected to the cosmic baryon asymmetry (Alexander, Peskin & Sheikh-Jabbari 2006; Alexander & Martin 2005; Alexander & Gates 2006). Since IGWs induce B modes only at multipole moments $\ell \lesssim 100$, the cosmic-variance limit to the sensitivity of any measurement to the chirality of the IGWs is significant, and the prospects to detect chiral gravitational waves are reasonable, only if the tensor-to-scalar ratio r is relatively large and if the chirality is significant (Gluscevic & Kamionkowski 2010; Ferté & Grain 2014).

9. Other paths to inflationary gravitational waves

There are other possibilities to detect inflationary gravitational waves. Although these are perhaps a bit further down the road than B modes, they may help characterize the gravitational-wave background, in case of detection, by complementing the CMB measurement, which probes gravitational waves with $\sim 10^{-17}$ Hz frequencies, with measurements at far higher frequencies (Smith, Kamionkowski & Cooray 2006; Chongchitnan & Efstathiou 2006; Smith, Kamionkowski & Cooray 2008). The idea to seek the inflationary background with gravitational-wave detectors was considered in Liddle (1994), Bar-Kana (1994), Turner (1997), Smith, Kamionkowski & Cooray (2006), Caldwell, Kamionkowski & Wadley (1999), and Smith, Kamionkowski & Cooray (2008), and has motivated mission concept studies for space-based gravitational-wave observatories like the Big-Bang Observer (Phinney et al. 2004; Crowder & Cornish 2005) and DECIGO (Seto, Kawamura & Nakamura 2001).

There is also the possibility to seek IGWs via their effects on the large-scale galaxy distribution. The gravitational-wave background may give rise to local quadrupolar departures from statistical isotropy in primordial perturbations (Maldacena 2003; Seery, Sloth & Vernizzi 2009; Giddings & Sloth 2011, 2012; Jeong & Kamionkowski 2012; Jeong & Schmidt 2012; Schmidt & Jeong 2012a; Bramante et al. 2013). It may also gravitationally lens the galaxy distribution (Dodelson, Rozo & Stebbins 2003; Masui & Pen 2010; Schmidt & Jeong 2012b; Schmidt, Pajer & Zaldarriaga 2014), the CMB (Cooray, Kamionkowski & Caldwell 2005; Li & Cooray 2006; Book, Kamionkowski & Souradeep 2012; Dodelson 2010; Dai, Kamionkowski & Jeong 2012; Dai, Jeong & Kamionkowski 2013b), or the 21-cm background (Pen 2004; Book, Kamionkowski & Schmidt 2012), affect the intrinsic alignments of elliptical galaxies (Schmidt, Pajer & Zaldarriaga 2014; Chisari, Dvorkin & Schmidt 2014; Schmidt, Chisari & Dvorkin 2015) via the tidal-alignment model (Catelan, Kamionkowski

& Blandford 2001), or have consequences for precision astrometry of quasars (Book & Flanagan 2011). These effects arise in SFSR inflation but are very small, at best. They may, however, be larger in solid inflation (Akhshik 2015; Dimastrogiovanni et al. 2014), non-attractor inflation (Dimastrogiovanni et al. 2014), quasi-single-field inflation (Dimastrogiovanni, Fasiello & Kamionkowski 2015), and globally-anisotropic models (Emami & Firouzjahi 2015). Strictly speaking, the precise distinction between early-time and late-time effects of gravitational waves on the galaxy distribution depends on the gauge choice, an issue explored and clarified in recent work (Dai, Jeong & Kamionkowski 2013a; Pajer, Schmidt & Zaldarriaga 2013; Dai, Pajer & Schmidt 2015).

A constraint to the primordial gravitational-wave amplitude at frequencies $\nu \gtrsim 10^{-11}$ Hz higher than those accessible with the CMB or large-scale structure can be obtained from big-bang nucleosynthesis (BBN) (Allen 1996)—such gravitational waves would act as an additional relativistic degree of freedom. This bound can then be extended to $\nu \gtrsim 10^{-15}$ Hz and improved with measurements of small-scale CMB fluctuations, which now improve upon the BBN bound to the number of relativistic degrees of freedom (Smith, Pierpaoli & Kamionkowski 2006; Sendra & Smith 2012; Pagano, Salvati & Melchiorri 2015). Still, these upper bounds are probably too weak to be constraining for SFSR inflation, although they may be of interest for models that predict a blue ($n_t > 0$) gravitational-wave spectrum (Brandenberger, Nayeri & Patil 2014).

10. Conclusions

We have described the quest for the B modes, the curl component of the CMB polarization, that arise from inflationary gravitational waves. Until recently, the lack of existing constraints to inflationary models allowed an almost arbitrarily small value for the tensor-to-scalar ratio r that parametrizes the strength of the B-mode signal. The plot has thickened in recent years, however, with measurements that show with increasing confidence that the scalar spectral index n_s departs from unity. Although model dependencies prevent an absolutely conclusive statement, single-field slow-roll models of inflation generally predict, with current constraints to n_s, values of r within striking distance of experimental capabilities on a 10-year timescale.

The challenge now will be to make these measurements, and a massive global effort is now underway. We summarized in Section 8 the issues that face experimentalists and the prospects for their resolution. There may also be room for new ideas (e.g., to cross-correlate the reionization-bump B modes with galaxy surveys (Alizadeh & Hirata 2012)), to facilitate the pursuit of inflationary gravitational waves.

Of course, if r is not too much smaller than the current upper bound $r \lesssim 0.09$ (from the combination of temperature and polarization constraints), then a detection may be just around the corner. If so, the obvious next step will be to characterize the gravitational-wave background through measurements of the spectral index n_t (Boyle et al. 2015; Huang, Wang & Zhao 2015), tests of the Gaussianity of these B modes, and the chirality of the GW background, and perhaps with complementary measurements of the gravitational-wave background at much smaller wavelengths.

The prospects for a fairly definitive test of the prevailing single-field slow-roll models of inflation have motivated considerable efforts in the pursuit of precise measurements of CMB polarization. The detection of a signal, if/when it occurs, will provide an entirely new window back to 10^{-38} seconds after the cosmic singularity; provide evidence, albeit indirect,

for interesting new physics at the GUT scale; constitute a detection of gravitational waves; and moreover, provide the first empirical information about the quantum behavior of the spacetime metric. All this may occur on a 10-year timescale, so pay attention!

DISCLOSURE STATEMENT

The authors have nothing to disclose.

ACKNOWLEDGMENTS

LITERATURE CITED

Abazajian KN, Arnold K, Austermann J, et al. 2015a. *Astropart. Phys.* 63:55 [arXiv:1309.5381]

Abazajian KN, Arnold K, Austermann J, et al. 2015b. *Astropart. Phys.* 63:66 [arXiv:1309.5383]

Abbott LF, Wise MB. 1984. *Nucl. Phys.* B244:541

Adam R, Ade PAR, Aghanim N, et al. 2014. arXiv:1409.5738

Adam R, Ade PAR, Aghanim N, et al. 2015a. arXiv:1502.01582

Adam R, Ade PAR, Aghanim N, et al. 2015b. arXiv:1502.05956

Adams FC, Bond JR, Freese K, Frieman JA, Olinto AV. 1993. *Phys. Rev.* D47:426 [arXiv:hep-ph/9207245]

Ade PAR, Akiba Y, Anthony AE, et al. 2014a. *Astrophys. J.* 794:171 [arXiv:1403.2369]

Ade PAR, Aikin RW, Amiri M, et al. 2014b. *Astrophys. J.* 792:62 [arXiv:1403.4302]

Ade PAR, Aikin RW, Barkats D, et al. 2014c. *Phys. Rev. Lett.* 112:241101 [arXiv:1403.3985]

Ade PAR, Akiba Y, Anthony AE, et al. 2014d. *Phys. Rev. Lett.* 112:131302 [arXiv:1312.6645]

Ade PAR, Aghanim N, Armitage-Caplan C, et al. 2014e. *Astron. Astrophys.* 571:A16 [arXiv:1303.5076]

Ade PAR, Aghanim N, Armitage-Caplan C, et al. 2014f. *Astron. Astrophys.* 571:A17 [arXiv:1303.5077]

Ade PAR, Aghanim N, Armitage-Caplan C, et al. 2014g. *Astron. Astrophys.* 571:A22 [arXiv:1303.5082]

Ade PAR, Aghanim N, Armitage-Caplan C, et al. 2014h. *Astron. Astrophys.* 571:A30 [arXiv:1309.0382]

Ade PAR, Alves MIR, Aniano G, et al. 2014i. *Astron. Astrophys.* 576:A107 [arXiv:1405.0874]

Ade PAR, Aghanim N, Alina D, et al. 2015a. *Astron. Astrophys.* 576:A106 [arXiv:1405.0873]

Ade PAR, Aghanim N, Ahmed Z, et al. 2015b. *Phys. Rev. Lett.* 114:101301 [arXiv:1502.00612]

Ade PAR, Ahmed Z, Aikin RW, et al. 2015c. arXiv:1502.00643

Ade PAR, Aghanim N, Arnaud M, et al. 2015d. arXiv:1502.01589

Ade PAR, Aghanim N, Arnaud M, et al. 2015e. arXiv:1502.02114

Adshead P, Martinec E, Wyman M. 2013. *JHEP* 09:087 [arXiv:1305.2930]

Aiola S, Amico G, Battalgia P et al. 2012. *Proc. SPIE* 8446:277 [arXiv:1208.0281]

Akhshik M. 2015. *JCAP* 1505:043 [arXiv:1409.3004]

Albrecht A, Steinhardt PJ. 1982. *Phys. Rev. Lett.* 48:1220

Alexander S, Martin J. 2005. *Phys. Rev.* D71:063526 [arXiv:hep-th/0410230]

Alexander S, Yunes N. 2009. *Phys. Rept.* 480:1 [arXiv:0907.2562]

Alexander SHS, Gates Jr. SJ. 2006. *JCAP* 0606:018 [arXiv:hep-th/0409014]

Alexander SHS, Peskin ME, Sheikh-Jabbari MM. 2006. *Phys. Rev. Lett.* 96:081301 [arXiv:hep-th/0403069]

Ali-Haimoud Y. 2013. *Adv. Astron.* 2013:462697 [arXiv:1211.2748]

Alishahiha M, Silverstein E, Tong D. 2004. *Phys. Rev.* D70:123505 [arXiv:hep-th/0404084]

Alizadeh E, Hirata CM. 2012. *Phys. Rev.* D85:123540 [arXiv:1201.5374]

Allen B. 1996. In *Relativistic gravitation and gravitational radiation. Proceedings, School of Physics, Les Houches, France, September 26-October 6, 1995* [arXiv:gr-qc/9604033]

Amendola L, Appleby S, Bacon D, et al. 2013. *Living Rev. Rel.* 16:6 [arXiv:1206.1225]

Andersson B-G, Lazarian A, Vaillancourt JE. 2015. *Ann. Rev. Astron. Astrophys.* 53:501

André P, Baccigalupi C, Banday A, et al. 2014. *JCAP* 1402:006 [arXiv:1310.1554]

Armendariz-Picon C, Damour T, Mukhanov VF. 1999. *Phys. Lett.* B458:209 [arXiv:hep-th/9904075]

Armitage-Caplan C, Avillez M, Barbosa D, et al. 2011. arXiv:1102.2181

Arnold K, Stebor N, Ade PAR, et al. 2014. *Conf. Ser. Pho.-Opt. Inst. Eng. (SPIE)* 9153:91531F

Bar-Kana R. 1994. *Phys. Rev.* D50:1157 [arXiv:astro-ph/9401050]

Bardeen JM, Steinhardt PJ, Turner MS. 1983. *Phys. Rev.* D28:679

Barnaby N, Moxon J, Namba R, et al. 2012. *Phys. Rev.* D86:103508 [arXiv:1206.6117]

Bartolo N, Komatsu E, Matarrese S, Riotto A. 2004. *Phys. Rept.* 402:103 [arXiv:astro-ph/0406398]

Battistelli E, Bau A, Bennett D, et al. 2012. *J. Low Temp. Phys.* 167:872 arXiv:1010.0645

Baumann D, Cooray A, Dodelson S, et al. 2009. *AIP Conf. Proc.* 1141:3 [arXiv:0811.3911]

Baumann D, McAllister L. 2009. *Ann. Rev. Nucl. Part. Sci.* 59:67 [arXiv:0901.0265]

Baumann D, McAllister L. 2015. *Inflation and String Theory.* Cambridge Univ. Press

Bennett CL, Larson D, Weiland JL, et al. 2013. *Astrophys. J. Suppl.* 208:20 [arXiv:1212.5225]

Benson BA, Ade PAR, Ahmed Z, et al. 2014. *Proc. SPIE* 9153:91531P [arXiv:1407.2973]

Bertschinger E. 1993. In *Summer School on Cosmology and Large Scale Structure (Session 60) Les Houches, France, August 1-28, 1993* [arXiv:astro-ph/9503125]

Bezrukov FL, Shaposhnikov M. 2008. *Phys. Lett.* B659:703-706 [arXiv:0710.3755]

Bielefeld J, Caldwell RR. 2015. *Phys. Rev.* D91:123501 [arXiv:1412.6104]

Birkinshaw M. 1999. *Phys. Rept.* 310:97 [arXiv:astro-ph/9808050]

Birrell ND, Davies PCW. 1984. *Quantum Fields in Curved Space.* Cambridge Monographs on Mathematical Physics. Cambridge Univ. Press

Bock J, Aljabri A, Amblard A, et al. 2009. arXiv:0906.1188

Book L, Kamionkowski M, Schmidt F. 2012. *Phys. Rev. Lett.* 108:211301 [arXiv:1112.0567]

Book LG, Flanagan EE. 2011. *Phys. Rev.* D83:024024 [arXiv:1009.4192]

Book LG, Kamionkowski M, Souradeep T. 2012. *Phys. Rev.* D85:023010 [arXiv:1109.2910]

Boyle L, Smith KM, Dvorkin C, Turok N. 2015. *Phys. Rev.* D92:043504 [arXiv:1408.3129]

Bramante J, Kumar J, Nelson E, Shandera S. 2013. *JCAP* 1311:021 [arXiv:1307.5083]

Brandenberger RH. 1985. *Rev. Mod. Phys.* 57:1

Brandenberger RH, Nayeri A, Patil SP. 2014. *Phys. Rev.* D90:067301 [arXiv:1403.4927]

Brout R, Englert F, Gunzig E. 1978. *Annals Phys.* 115:78

Buchmuller W, Domcke V, Kamada K. 2013. *Phys. Lett.* B726:467 [arXiv:1306.3471]

Buonanno A, Sathyaprakash BS. 2014 arXiv:1410.7832

Cabella P, Kamionkowski M. 2004. In *Int. School of Grav. and Cos.: The Polarization of the Cosmic Microwave Background Rome, Italy, September 6-11, 2003* [arXiv:astro-ph/0403392]

Calabrese E, Hlozek RA, Battaglia N, et al. 2013. *Phys. Rev.* D87:103012 [arXiv:1302.1841]

Caldwell RR, Kamionkowski M, Wadley L. 1999. *Phys. Rev.* D59:027101 [arXiv:astro-ph/9807319]

Carney D, Fischler W, Kovetz ED, Lorshbough D, Paban S. 2012. *JHEP* 11:042 [arXiv:1209.3848]

Catelan P, Kamionkowski M, Blandford RD. 2001. *Mon. Not. Roy. Astron. Soc.* 320:L7 [arXiv:astro-ph/0005470]

Chisari, NE, Dvorkin C, Schmidt, F. 2014. *Phys. Rev.* D90:043527 [arXiv:1406.4871]

Chongchitnan S, Efstathiou G. 2006. *Phys. Rev.* D73:083511 [arXiv:astro-ph/0602594]

Clifton T, Ferreira PG, Padilla A, Skordis C. 2012. *Phys. Rept.* 513:1 [arXiv:1106.2476]

Coleman SR, Weinberg EJ. 1973. *Phys. Rev.* D7:1888

Contaldi CR, Magueijo J, Smolin L. 2008. *Phys. Rev. Lett.* 101:141101 [arXiv:0806.3082]

Cook JL, Dimastrogiovanni E, Easson DA, Krauss LM. 2015. *JCAP* 1504:047 [arXiv:1502.04673]

Cook JL, Sorbo L. 2012. *Phys. Rev.* D85:023534. [Erratum: Phys. Rev.D86,069901(2012)] [arXiv:1109.0022]

Cooray A, Kamionkowski M, Caldwell RR. 2005. *Phys. Rev.* D71:123527 [arXiv:astro-ph/0503002]

Creminelli P, Nacir DL, Simonović M, Trevisan G, Zaldarriaga M. 2015. arXiv:1502.01983

Crill BP, Ade PAR, Battistelli ES, et al. 2008. *Proc. SPIE* 7010:2P [arXiv:0807.1548]

Crittenden RG. 1993. PhD Thesis, University of Pennsylvania

Crittenden R, Davis RL, Steinhardt PJ. 1993. *Astrophys. J.* 417:L13 [arXiv:astro-ph/9306027]

Crittenden RG, Coulson D, Turok NG. 1995. *Phys. Rev.* D52:5402 [arXiv:astro-ph/9411107]

Crowder J, Cornish NJ. 2005. *Phys. Rev.* D72:083005 [arXiv:gr-qc/0506015]

Dai L, Jeong D, Kamionkowski M. 2013a. *Phys. Rev.* D88:043507 [arXiv:1306.3985]

Dai L, Jeong D, Kamionkowski M. 2013b. *Phys. Rev.* D87:103006 [arXiv:1302.1868]

Dai L, Kamionkowski M, Jeong D. 2012. *Phys. Rev.* D86:125013 [arXiv:1209.0761]

Dai L, Kamionkowski M, Wang J. 2014. *Phys. Rev. Lett.* 113:041302 [arXiv:1404.6704]

Dai L, Pajer E, Schmidt F. 2015. [arXiv:1502.02011]

Das S, Sherwin BD, Aguirre P, et al. 2011. *Phys. Rev. Lett.* 107:021301 [arXiv:1103.2124]

Dawson KS, Schlegel DJ, Ahn CP, et al. 2013. *Astron. J.* 145:10 [arXiv:1208.0022]

De Felice A, Tsujikawa S. 2011. *JCAP* 1104:029 [arXiv:1103.1172]

Delabrouille J, Betoule M, Melin JB, et al. 2013. *Astron. Astrophys.* 553:A96 [arXiv:1207.3675]

Dicus DA, Repko WW. 2005. *Phys. Rev.* D72:088302 [arXiv:astro-ph/0509096]

Dimastrogiovanni E, Fasiello M, Jeong D, Kamionkowski M. 2014. *JCAP* 1412:050 [arXiv:1407.8204]

Dimastrogiovanni E, Fasiello M, Kamionkowski M. 2015. arXiv:1504.05993

Dimopoulos S, Raby S, Wilczek F. 1981. *Phys. Rev.* D24:1681

Dodelson S. 2003. *Modern Cosmology*. Amsterdam: Academic Press

Dodelson S. 2010. *Phys. Rev.* D82:023522 [arXiv:1001.5012]

Dodelson S, Rozo E, Stebbins A. 2003. *Phys. Rev. Lett.* 91:021301 [arXiv:astro-ph/0301177]

Draine BT, Fraisse AA. 2009. *Astrophys. J.* 696:1. [Erratum: Astrophys. J.757,106(2012)] [arXiv:0809.2094]

Draine BT, Hensley B. 2013. *Astrophys. J.* 765:159 [arXiv:1205.7021]

Ellis J, Nanopoulos DV, Olive KA. 2013. *Phys. Rev. Lett.* 111:111301. [Erratum: Phys. Rev. Lett.111,no.12,129902(2013)] [arXiv:1305.1247]

Emami R, Firouzjahi H. 2015. arXiv:1506.00958

Essinger-Hileman T, Ali A, Amiri M, et al. 2014. *Proc. SPIE* 9153:91531I [arXiv:1408.4788]

Fabbri R, Pollock Md. 1983. *Phys. Lett.* B125:445

Ferté A, Grain J. 2014. *Phys. Rev.* D89:103516 [arXiv:1404.6660]

Flauger R, Hill JC, Spergel DN. 2014. *JCAP* 1408:039 [arXiv:1405.7351]

Flauger R, Weinberg S. 2007. *Phys. Rev.* D75:123505 [arXiv:astro-ph/0703179]

Freese K, Kinney WH. 2015. *JCAP* 1503:044 [arXiv:1403.5277]

Giddings SB, Sloth MS. 2011. *JCAP* 1101:023 [arXiv:1005.1056]

Giddings SB, Sloth MS. 2012. *Phys. Rev.* D86:083538 [arXiv:1109.1000]

Gluscevic V, Kamionkowski M. 2010. *Phys. Rev.* D81:123529 [arXiv:1002.1308]

Guth AH. 1981. *Phys. Rev.* D23:347

Guth AH, Pi SY. 1982. *Phys. Rev. Lett.* 49:1110

Hanson D, Hoover S, Crites A, et al. 2013. *Phys. Rev. Lett.* 111:141301 [arXiv:1307.5830]

Harrison ER. 1970. *Phys. Rev.* D1:2726

Haslam CGT, Salter CJ, Stoffel H, Wilson WE. 1982. *Astron. Astrophys. Supp.* 47:1

Hawking SW. 1975. *Commun. Math. Phys.* 43:199

Hawking SW. 1982. *Phys. Lett.* B115:295

Hirata CM, Ho S, Padmanabhan N, Seljak U, Bahcall NA. 2008. *Phys. Rev.* D78:043520 [arXiv:0801.0644]

Hirata CM. 2014. `http://tinyurl.com/oy8d2dk`

Hu W, Dodelson S. 2002. *Ann. Rev. Astron. Astrophys.* 40:171 [arXiv:astro-ph/0110414]

Hu W, Hedman MM, Zaldarriaga M. 2003. *Phys. Rev.* D67:043004 [arXiv:astro-ph/0210096]

Hu W, Okamoto T. 2002. *Astrophys. J.* 574:566 [arXiv:astro-ph/0111606]

Hu W, White MJ. 1997a. *New Astron.* 2:323 [arXiv:astro-ph/9706147]

Hu W, White MJ. 1997b. *Phys. Rev.* D56:596 [arXiv:astro-ph/9702170]

Huang QG, Wang S, Zhao W. 2015 arXiv:1509.02676

Itzhaki N, Kovetz ED. 2007. *JHEP* 10:054 [arXiv:0708.2798]

Itzhaki N, Kovetz ED. 2009. *Class. Quant. Grav.* 26:135007 [arXiv:0810.4299]

Jackiw R, Pi SY. 2003. *Phys. Rev.* D68:104012 [arXiv:gr-qc/0308071]

Jaffe AH, Kamionkowski M, Wang LM. 2000. *Phys. Rev.* D61:083501 [arXiv:astro-ph/9909281]

Jeong D, Kamionkowski M. 2012. *Phys. Rev. Lett.* 108:251301 [arXiv:1203.0302]

Jeong D, Schmidt F. 2012. *Phys. Rev.* D86:083512 [arXiv:1205.1512]

Jungman G, Kamionkowski M, Kosowsky A, Spergel DN. 1996. *Phys. Rev.* D54:1332 [arXiv:astro-ph/9512139]

Kachru S, Kallosh R, Linde AD, Trivedi SP. 2003. *Phys. Rev.* D68:046005 [arXiv:hep-th/0301240]

Kamionkowski M, Kosowsky A. 1998. *Phys. Rev.* D57:685 [arXiv:astro-ph/9705219]

Kamionkowski M, Kosowsky A. 1999. *Ann. Rev. Nucl. Part. Sci.* 49:77 [arXiv:astro-ph/9904108]

Kamionkowski M, Kosowsky A, Stebbins A. 1997a. *Phys. Rev. Lett.* 78:2058 [arXiv:astro-ph/9609132]

Kamionkowski M, Kosowsky A, Stebbins A. 1997b. *Phys. Rev.* D55:7368 [arXiv:astro-ph/9611125]

Kamionkowski M, Kovetz ED. 2014. *Phys. Rev. Lett.* 113:191303 [arXiv:1408.4125]

Kaplan DE, Weiner NJ. 2004. *JCAP* 0402:005 [arXiv:hep-ph/0302014]

Katayama N, Komatsu E. 2011. *Astrophys. J.* 737:78 [arXiv:1101.5210].

Kazanas D. 1980. *Astrophys. J.* 241:L59

Keating B, Ade PAR, Bock JJ, et al. 2003. *Proc. SPIE* 4843:284

Keisler R, Hoover S, Harrington N, et al. 2015. *Astrophys. J.* 807:151 [arXiv:1503.02315]

Kesden M, Cooray A, Kamionkowski M. 2002. *Phys. Rev. Lett.* 89:011304 [arXiv:astro-ph/0202434]

Kesden MH, Cooray A, Kamionkowski M. 2003. *Phys. Rev.* D67:123507 [arXiv:astro-ph/0302536]

Kinney WH. 2015. private communication

Kinney WH, Mahanthappa KT. 1996. *Phys. Rev.* D53:5455 [arXiv:hep-ph/9512241]

Kleban M, Mirbabayi M, Porrati M. 2015. arXiv:1508.01527

Knox L. 1995. *Phys. Rev.* D52:4307 [arXiv:astro-ph/9504054]

Knox L, Song YS. 2002. *Phys. Rev. Lett.* 89:011303 [arXiv:astro-ph/0202286]

Knox L, Turner MS. 1993. *Phys. Rev. Lett.* 70:371 [arXiv:astro-ph/9209006]

Kodama H, Sasaki M. 1984. *Prog. Theor. Phys. Suppl.* 78:1

Kogut A, Hinshaw G, Banday AJ, et al. 1996. *Astrophys. J.* 464:L5 [arXiv:astro-ph/9601060]

Kogut A, Fixsen DJ, Chuss DT, et al. 2011. *JCAP* 7:025 [arXiv:1105.2044]

Komatsu E, Dunkley J, Nolta MR, et al. 2009. *Astrophys. J. Suppl.* 180:330 [arXiv:0803.0547]

Kosowsky A. 1996. *Annals Phys.* 246:49 [arXiv:astro-ph/9501045]

Kosowsky A, Turner MS. 1995. *Phys. Rev.* D52:1739 [arXiv:astro-ph/9504071]

Kovetz ED, Kamionkowski M. 2015. *Phys. Rev.* D91:081303 [arXiv:1502.00625]

Kovetz ED, Kamionkowski M. 2016. *New Astron.* 43:26 [arXiv:1308.1404]

La D, Steinhardt PJ. 1989. *Phys. Rev. Lett.* 62:376. [Erratum: Phys. Rev. Lett.62,1066(1989)]

Lazear J, Ade PAR, Benford D, et al. 2014. *Proc. SPIE* 9153:91531L [arXiv:1407.2584]

Leitch EM, Readhead ACS, Pearson TJ, Myers ST. 1997. *Astrophys. J.* 486:L23 [arXiv:astro-ph/9705241]

Lewis A, Challinor A. 2006. *Phys. Rept.* 429:1 [arXiv:astro-ph/0601594]

Lewis A, Challinor A, Lasenby A. 2000. *Astrophys. J.* 538:473 [arXiv:astro-ph/9911177]

Lewis A, Challinor A, Turok N. 2002. *Phys. Rev.* D65:023505 [arXiv:astro-ph/0106536]

Li C, Cooray A. 2006. *Phys. Rev.* D74:023521 [arXiv:astro-ph/0604179]

Liddle AR. 1994. *Phys. Rev.* D49:3805. [Erratum: Phys. Rev.D51,4603(1995)] [arXiv:gr-qc/9307036]

Liddle AR, Lyth DH. 2000. *Cosmological inflation and large scale structure.* Cambridge Univ. Press

Lidsey JE, Liddle AR, Kolb EW, et al. 1997. *Rev. Mod. Phys.* 69:373 [arXiv:astro-ph/9508078]

Linde AD. 1982a. *Phys. Lett.* B108:389

Linde AD. 1982b. *Phys. Lett.* B116:335

Linde AD. 1983. *Phys. Lett.* B129:177

Lue A, Wang LM, Kamionkowski M. 1999. *Phys. Rev. Lett.* 83:1506 [arXiv:astro-ph/9812088]

Lyth DH. 1997. *Phys. Rev. Lett.* 78:1861 [arXiv:hep-ph/9606387]

Lyth DH, Riotto A. 1999. *Phys. Rept.* 314:1 [arXiv:hep-ph/9807278]

Ma CP, Bertschinger E. 1995. *Astrophys. J.* 455:7 [arXiv:astro-ph/9506072]

Maldacena JM. 2003. *JHEP* 05:013 [arXiv:astro-ph/0210603]

Maleknejad A, Sheikh-Jabbari MM, Soda J. 2013. *Phys. Rept.* 528:161 [arXiv:1212.2921]

Malik KA, Wands D. 2009. *Phys. Rept.* 475:1 [arXiv:0809.4944]

Marian L, Bernstein GM. 2007. *Phys. Rev.* D76:123009 [arXiv:0710.2538]

Martin PG. 1971. *Mon. Not. Roy. Astron. Soc.* 153:279

Martin J, Ringeval C, Vennin V. 2014. *Phys. Dark Univ.* 5-6:75 [arXiv:1303.3787]

Masui KW, Pen UL. 2010. *Phys. Rev. Lett.* 105:161302 [arXiv:1006.4181]

Matsumura T, Akiba Y, Borrill J, et al. 2013. *J. Low Temp. Phys.* 176:733 arXiv:1311.2847

Mazumdar A, Rocher J. 2011. *Phys. Rept.* 497:85 [arXiv:1001.0993]

McAllister L, Silverstein E, Westphal A. 2010. *Phys. Rev.* D82:046003 [arXiv:0808.0706]

Mirbabayi M, Senatore L, Silverstein E, Zaldarriaga M. 2015. *Phys. Rev.* D91:063518 [arXiv:1412.0665]

Mortonson MJ, Seljak U. 2014. *JCAP* 1410:035 [arXiv:1405.5857]

Mukhanov V. 2005. *Physical Foundations of Cosmology.* Cambridge Univ. Press

Mukhanov VF, Chibisov GV. 1981. *JETP Lett.* 33:532 [Pisma Zh. Eksp. Teor. Fiz.33,549(1981)]

Mukhanov VF, Feldman HA, Brandenberger RH. 1992. *Phys. Rept.* 215:203

Munoz JB, Kamionkowski M. 2015. *Phys. Rev.* D91:043521 [arXiv:1412.0656]

Naess S, Hasselfield M, McMahon J, et al. 2014. *JCAP* 1410:007 [arXiv:1405.5524]

Ng KL, Ng KW. 1996. *Astrophys. J.* 456:413 [arXiv:astro-ph/9412097]

O'Dea DT, Clark CN, Contaldi CR, MacTavish CJ. 2012. *Mon. Not. Roy. Astron. Soc.* 419:1795 [arXiv:1107.4612]

Olive KA. 1990. *Phys. Rept.* 190:307

Özsoy O, Sinha K, Watson S. 2015. *Phys. Rev.* D91:103509 [arXiv:1410.0016]

Pagano L, Salvati L, Melchiorri A. 2015. arXiv:1508.02393

Page L, Hinshaw G, Komatsu E, et al. 2007. *Astrophys. J. Suppl.* 170:335 [arXiv:astro-ph/0603450]

Pajer E, Schmidt F, Zaldarriaga M. 2013. *Phys. Rev.* D88:083502 [arXiv:1305.0824]

Pearson R, Sherwin B, Lewis A. 2014. *Phys. Rev.* D90:023539 [arXiv:1403.3911]

Peebles PJE, Yu JT. 1970. *Astrophys. J.* 162:815

Pen UL. 2004. *New Astron.* 9:417 [arXiv:astro-ph/0305387]

Phinney ES, et al., 2004. *The Big bang observer: Direct detection of gravitational waves from the birth of the Universe to the Present,* NASA Mission Concept Study

Polnarev AG. 1986. *Sov. Astron.* 29:607

Preskill J. 1979. *Phys. Rev. Lett.* 43:1365

Pritchard JR, Kamionkowski M. 2005. *Annals Phys.* 318:2 [arXiv:astro-ph/0412581]

Rees MJ. 1968. *Astrophys. J. Lett.* 153:L1

Reichborn-Kjennerud B, Aboobaker AM, Ade PAR, et al. 2010. *Proc. SPIE* 7741:1C [arXiv:1007.3672]

Remazeilles M, Dickinson C, Eriksen HKK, Wehus IK. 2015. arXiv:1509.04714

Rubakov VA, Sazhin MV, Veryaskin AV. 1982. *Phys. Lett.* B115:189

Samtleben D, Staggs S, Winstein B. 2007. *Ann. Rev. Nucl. Part. Sci.* 57:245 [arXiv:0803.0834]

Sato K. 1981. *Mon. Not. Roy. Astron. Soc.* 195:467

Schmidt F, Jeong D. 2012a. *Phys. Rev.* D86:083527 [arXiv:1204.3625]

Schmidt F, Jeong D. 2012b. *Phys. Rev.* D86:083513 [arXiv:1205.1514]

Schmidt F, Pajer E, Zaldarriaga M. 2014. *Phys. Rev.* D89:083507 [arXiv:1312.5616]

Schmidt F, Chisari NE, Dvorkin C. 2015. arXiv:1506.02671

Seery D, Sloth MS, Vernizzi F. 2009. *JCAP* 0903:018 [arXiv:0811.3934]

Seljak U. 1997. *Astrophys. J.* 482:6 [arXiv:astro-ph/9608131]

Seljak U, Hirata CM. 2004. *Phys. Rev.* D69:043005 [arXiv:astro-ph/0310163]

Seljak U, Zaldarriaga M. 1996. *Astrophys. J.* 469:437 [arXiv:astro-ph/9603033]

Seljak U, Zaldarriaga M. 1997. *Phys. Rev. Lett.* 78:2054 [arXiv:astro-ph/9609169]

Seljak U, Zaldarriaga M. 1999. *Phys. Rev. Lett.* 82:2636 [arXiv:astro-ph/9810092]

Senatore L, Silverstein E, Zaldarriaga M. 2014. *JCAP* 1408:016 [arXiv:1109.0542]

Sendra I, Smith TL. 2012. *Phys. Rev.* D85:123002 [arXiv:1203.4232]

Seto N, Kawamura S, Nakamura T. 2001. *Phys. Rev. Lett.* 87:221103 [arXiv:astro-ph/0108011]

Sherwin BD, Schmittfull M. 2015. *Phys. Rev.* D92:043005 [arXiv:1502.05356]

Sigurdson K, Cooray A. 2005. *Phys. Rev. Lett.* 95:211303 [arXiv:astro-ph/0502549]

Silverstein E, Westphal A. 2008. *Phys. Rev.* D78:106003 [arXiv:0803.3085]

Simard G, Hanson D, Holder G. 2015. *Astrophys. J.* 807:166 [arXiv:1410.0691]

Smith KM. 2005 *Phys. Rev.* D74:083002 [arXiv:astro-ph/0511629]

Smith KM, Hanson D, LoVerde M, Hirata CM, Zahn O. 2012. *JCAP* 1206:014 [arXiv:1010.0048]

Smith KM, Zahn O, Dore O. 2007. *Phys. Rev.* D76:043510 [arXiv:0705.3980]

Smith TL, Kamionkowski M, Cooray A. 2006. *Phys. Rev.* D73:023504 [arXiv:astro-ph/0506422]

Smith TL, Kamionkowski M, Cooray A. 2008. *Phys. Rev.* D78:083525 [arXiv:0802.1530]

Smith TL, Pierpaoli E, Kamionkowski M. 2006. *Phys. Rev. Lett.* 97:021301 [arXiv:astro-ph/0603144]

Staggs S, et. al. 2015. `http://www.princeton.edu/physics/research/cosmology-experiment/abs-experiment/`

Starobinsky AA. 1979. *JETP Lett.* 30:682 [Pisma Zh. Eksp. Teor. Fiz.30,719(1979)]

Starobinsky AA. 1980. *Phys. Lett.* B91:99

Starobinsky AA. 1982. *Phys. Lett.* B117:175

Sunyaev RA, Zeldovich YaB. 1972. *Comments Astrophys. Space Phys.* 4:173

Sunyaev RA, Zeldovich YaB. 1980. *Ann. Rev. Astron. Astrophys.* 18:537

Takahashi T, Soda J. 2009. *Phys. Rev. Lett.* 102:231301 [arXiv:0904.0554]

Turner MS. 1993. *Phys. Rev.* D48:5539 [arXiv:astro-ph/9307035]

Turner MS. 1997. *Phys. Rev.* D55:435 [arXiv:astro-ph/9607066]

Turner MS, Wilczek F. 1991. *Phys. Rev. Lett.* 66:5

van Engelen A, Keisler R, Zahn O, et al. 2012. *Astrophys. J.* 756:142 [arXiv:1202.0546]

van Engelen A, Sherwin BD, Sehgal N, et al. 2015. *Astrophys. J.* 808:7 [arXiv:1412.0626]

Verde L, Peiris H, Jimenez R. 2006. *JCAP* 0601:019 [arXiv:astro-ph/0506036]

Watts DJ, Larson D, Marriage TA, et al. 2015. arXiv:1508.00017

Weinberg S. 2004. *Phys. Rev.* D69:023503 [arXiv:astro-ph/0306304]

Weinberg S. 2008. *Cosmology.* Oxford Univ. Press

Westphal A. 2015. *Int. J. Mod. Phys.* A30:1530024 [arXiv:1409.5350]

Wu WLK, Errard J, Dvorkin C, et al. 2014. *Astrophys. J.* 788:138 [arXiv:1402.4108]

Zaldarriaga M. 1997. *Phys. Rev.* D55:1822 [arXiv:astro-ph/9608050]

Zaldarriaga M. 2001. *Phys. Rev.* D64:103001 [arXiv:astro-ph/0106174]

Zaldarriaga M, Harari DD. 1995. *Phys. Rev.* D52:3276 [arXiv:astro-ph/9504085]

Zaldarriaga M, Seljak U. 1997. *Phys. Rev.* D55:1830 [arXiv:astro-ph/9609170]

Zaldarriaga M, Seljak U. 1998. *Phys. Rev.* D58:023003 [arXiv:astro-ph/9803150]

Zaldarriaga M, Seljak U. 1999. *Phys. Rev.* D59:123507 [arXiv:astro-ph/9810257]

Zeldovich YaB. 1970. *Astron. Astrophys.* 5:84